Recovery of atmospheric water vapor total column abundance from imaging spectrometer data around 940 nm - Sensitivity analysis and application to Airborne Visible/Infrared imaging Spectrometer (AVIRIS) data.

VERONIQUE CARRERE and JAMES E. CONEL

Jet Propulsion Laboratory, California Institute of Technology, M.S. 183-501, 4800 *Oak Grove Drive, Pasadena, CA* 91109, *USA*

Two simple techniques to retrieve path precipitable water from the Airborne Visible/Infrared Imaging Spectrometer (AVIRIS) high spectral resolution radiance data (Continuum Interpolated Band Ratio, CIBR, and Narrow/Wide ratio, N/W), using the 94o nm water absorption band, are compared. Since the shape and depth of the atmospheric water bands are influenced not only by the water present but also by surface (background) reflectance, atmospheric scattering, and instrument radiance by calibration, a sensitivity analysis was performed using the radiative transfer code LOWTRAN 7 (Kneizys et al., 1988) to determine which one of these two approaches will provide a better estimate over land and water areas. The CIBR proved to be the technique less sensitive to perturbing effects, except for errors in visibility estimate. Both techniques were applied to AVIRIS radiance data acquired over Salton Sea, California. Resulting images confirmed that the use of a constant gray reflectance in the model lead to a higher overestimation of the amount of water retrieved for N/W over vegetated areas. Validation was performed through comparison between an independent estimate of water vapor from concurrent Reagan sunphotometer measurements, and AVIRIS estimates. Amounts retrieved using the N/W approach match more closely in-situ measurements, even after adjusting model parameters for background reflectance,

viewing geometry and type of aerosol at the site. The 13% underestimation observed for the CIBR was explained by small differences $\Delta L(\lambda_i)$ between AVIRIS and LOWTRAN 7 modeled radiances. Results from this study emphasizes the importance of accurate instrument calibration in flight and physical modeling of atmospheric absorption.

INTRODUCTION

Water vapor is a key driver to global atmospheric circulation. As such, it is of interest in studies involving weather and climate modeling, and the hydrologic cycle. in addition, water vapor band and continuum absorption provide substantial obstacles to remote sensing of the Earth's surface in the 400-2500 nm region. Such observations seek to recover surface spectral reflectance or surface leaving spectral radiance. Accurate water vapor measurements are required to assess atmospheric heating rates, the redistribution of latent heat by the atmosphere accompanying water vapor transport, and the effect of water vapor attenuation. The goal of the present paper is to give a reasonably complete error and sensitivity anaiysis of simple ratio algorithms used with Airborne Visibie/infrared Imaging Spectrometer (AVIRIS) observations to determine the column abundance of atmospheric water vapor. AVIRIS measures upwelling radiance of the Earth's surface between 400-2450 nm at a spectral resolution of 10 nm, a spatial resolution of 20 m and with rapid areal coverage (about 100 km^2 in 40 sec.). With this capability, the instrument provides an important calibration and validation link between point observations of column water vapor abundance made from the surface using sunphotometers, microwave radiometers or radiosondes, and observations made by large footprint satellite sensors. AVIRIS can aiso serve under field conditions to validate water vapor column abundance distributions produced from theoretical models of atmospheric water vapor transport. in our approach, the sunphotometer-based water retrievals are fundamentally linked to laboratory spectroscopic measurements of water

vapor absorption via retrievals based on inversions of single water vapor lines made with an interferometer (Bruegge et al., 1992).

Fowle (1912, 1913) early demonstrated that it was possible to measure atmospheric water amounts in the infrared part of the spectrum using a differential absorption concept consisting of viewing a source of radiant energy at two or more wavelengths within and outside of a water vapor absorption band through the same atmospheric path. Since then, such spectroscopic methods have been applied and verified in many studies (Hand, 1940; Gates, 1956; Reagan et al., 1987, for example). The differential absorption technique has been extended here to imaging spectrometer data such as those acquired by AVIRIS.

OVERVIEW OF THE INVESTIGATION

We will analyze systematic and random sources of error present when retrieving path precipitable water abundances from AVIRIS data. The analysis will be confined to the 940 nm atmospheric water absorption band. The 940 nm water band was selected because it is the most sensitive of any of the unsaturated near-infrared bands to changes in amount of water present in the atmosphere. For retrievals of water vapor over the land and water surfaces, two simple algorithms are compared: (1) the Continuum interpolated Band Ratio (CIBR, Green et al., 1990a), and (2) the Narrow/Wide. ratio (N/W, Frouin and Middleton, 1990; Frouin et al., 1990). Both of these algorithms are implemented using the radiative transfer code LOWTRAN 7 (Kneizys et al., 1988) for calculation of the spectral radiance at AVIRIS. Implementation of LOWTRAN 7 requires specification of: (1) surface (Lambertian) spectral reflectance, (2) the water vapor column abundance W in g/cm^2, (3) aerosol loading in the atmospheric boundary layer (o - 2 km) parameterized as the surface meteorological range V (km^{-1}), (4) the aerosol scattering model A , (5) geometry of the solar incidence (O., φ_o) and viewing

(θ, φ) directions for points in the AVIRIS image at the time of the overflight (θ being zenith angle and φ azimuth), and (6) altitude of the surface above sea level h. In (2) and (3) above, we have assumed the standard vertical distributions provided with the geographical-seasonal model used, e. g., mid-latitude summer. The total water vapor column abundance has simply been scaled as needed as a multiple f ($0 \leq f \leq 2$) of the standard column abundance present, without changing the functional form of the resident vertical distribution. The spectral aerosol extinction coefficients were also left independent of any humidity changes implied by scaling the total water abundance. This latter assumption affects the aerosol size distribution, but does not appear to introduce any serious changes in the magnitudes or shapes of the (backward scattering portions of) phase functions used in our applications.

Water vapor calibration laws were developed that represent relationships between upwelling spectral radiance at AVIRIS, the column water abundance, and other model parameters, just listed. Systematic errors will appear in retrievals as unreal variations in water vapor amounts whenever the actual atmospheric or other conditions encountered differ from those assumed in the model. We evaluated the magnitudes of such errors by simulations with LOWTRAN 7 implemented as follows. (1) A calibration law was developed for the following 'reference" or standard conditions: latitude 33.2 N, longitude 115.5 W, 18 April, 11:05 PST corresponding to a solar zenith angle of 24.6 deg., 25 km surface meteorological range, rural aerosol model, target at sea level, observer at an altitude of 20 km, flight direction north, nadir viewing, and a constant (spectrally gray) surface reflectance of 25%. (2) Each of these parameters was varied one at a time from its reference value. For example, the background reflectance was changed systematically by substitution of laboratory reflectance spectra of soils and vegetation. (3) The resulting aitered water calibration laws were compared to the

calibration law developed for the reference conditions to assess magnitudes of the systematic errors introduced in the amounts of water retrieved.

Following these studies, which focussed on problems with the LOWTRAN 7-based calibration laws, we investigated the role of AVIRIS, specifically systematic impacts arising from uncertainties in the inflight spectral and radiometric calibrations of the instrument. Next, we evaluated random errors, which were taken to originate from instrument noise. These uncertainties were calculated by straightforward application of error propagation analysis to the algorithms themselves.

Finally we applied these ideas to three AVIRIS data sets acquired at Salton Sea, California, and attempted to disentangle various sources of disagreement that were found to emerge between the retrievals generated from each algorithm and the water vapor variation observed with a sunphotometer at one point on the ground.

ALGORITHMS

Both the CIBR and N/W algorithms are attractive for the analysis of atmospheric water vapor because they are computationally rapid and easy to apply to AVIRIS data. Both retrieve the total water vapor abundance over combined downward and upward slant paths through the atmosphere from *sun* to sensor. The local water vapor column abundance W_n, in precipitable cm, along a direction normal to the surface is presently obtained under an assumption of local horizontal atmospheric homogeneity of the water distribution over these paths such that

$$W_n = W_T \left(\frac{1}{\cos \theta_0} + \frac{1}{\cos \theta} \right)^{-1}, \qquad (1)$$

where W_T is the total water abundance derived from the AVIRIS radiances by either algorithm. The θ and θ_0 angles are known for every image pixel from the path and time of AVIRIS overflight.

Continuum Interpolated Band Ratio (CIBR) Algorithm

The CIBR algorithm uses radiance measurements at the center of an absorption band, together with values of the 'continuum" radiances to either side (Figure la). A value of the continuum radiance at the wavelength of maximum water band absorption is estimated by linear interpolation between two adjacent continuum values. A ratio is formed between the interpolated continuum and band radiances:

$$CIBR = L/(AC_1+BC_2), \qquad (2)$$

where L is the band interpolated radiance, Cl and C_2 are the continuum radiances (Figure 1a), and A and B are weighting constants, equal to 0.5 at 940 nm where the continuum radiances are symmetrically positioned in wavelength to either side of the wavelength of L. These radiances, calculated at 1.8 nm spectral resolution by LOWTRAN 7, are each weighted by the AVIRIS channel spectral response functions. These response functions are close to Gaussian in shape with a full width at half maximum response close to 10 nm (Chrien et al., 1990; Green et al., 1990b). A CIBR value is generated for each amount of water, and a file created, that relates water amount to the radiance ratio. The resulting calibration law has the approximate form

$$CIBR = \exp[-\alpha W^{\beta}], \qquad (3)$$

where W is the total path water in cm, W_T in Equation (l), and a and β are parameters, which are function of ail the model variables. Supplying the spectral radiances calculated by LOWTRAN 7 to Equation (3) leads to small differences (about 1% low) in the value of W obtained from those assumed in the model (Figure 2a, 2c). These differences arise from the single exponential term approximation used in the least square fits as represented in Equation (3). Improved forms for the CIBR can be generated by including higher powers lnk(W) in the fits up to k=3. The double exponential logarithmic polynomial expressions that result are analytically cumbersome. The extra terms have not been included in the present analysis to avoid this complexity.

Narrow/Wide Band Ratio (N/W) Algorithm

This algorithm, as formulated by Frouin et al. (1990), uses two spectral channels (Figure 1 b), one narrow, the other wide, centered on the same wavelength at the water vapor absorption maximum in the 940 nm water vapor band. In the specific case of AVIRIS data, an average of three AVIRIS bands between 935 and 955 nm was used for the narrow band and of seven bands from 920 to 970 nm for the wide band:

$$\frac{N}{W} = \frac{\sim \quad L_j \ /3}{\sum_{j=1}^{7} L_j \ /7} \qquad (4)$$

Using LOWTRAN 7, a calibration curve is built in a way similar to that for the CIBR. The N/W calibration law follows the same exponential form as given by Equation (2), but with different values of α and β (Figure 1 c).

Assigning spectral radiances generated by LOWTRAN 7 for specific water abundances to Equation(4) leads to differences in derived water abundances from those assured in the model on the order of 3% (low) (Figure 2b, 2c). These differences can also be eliminated by inclusion of additional terms $\ln^k(W)$ in the least square fits but have also been excluded in the present analyses to avoid the resulting analytical complexity.

SYSTEMATIC ERRORS FROM CALIBRATION MODEL ASSUMPTIONS

Any departures of actual flight instrumental and/or atmospheric or surface conditions from those assumed in construction of the model-derived water vapor calibration laws for CIBR and N/W algorithms give rise to unreal water vapor variation, i. e., systematic errors in the derived abundances. Systematic errors based on simulations with LOWTRAN 7 are presented as fractional differences between the amounts of water retrieved using the 'reference' calibration relationship and amounts derived from altered relationships representing departures from the standard conditions. The fractional water difference $\Delta W/W$ between reference and altered conditions is defined as:

$$\frac{\Delta W}{W} = \frac{(W_{ref} - W_x)}{W_{ref}}, \qquad (5)$$

where W_{ref} is the column water abundance, derived from the standard or reference conditions, and W_x is that derived by varying parameter x in the standard model. Thus $\Delta W/W > 0$ means the derived water abundance under the altered conditions is less than that calculated under the standard model and conversely.

Written out in full, Equation (3) becomes

$$\frac{\Delta W}{w} = 1 - [- \ln (y_{std})]^{(1/\beta(x) - 1/\beta(ref))} \frac{\alpha(ref)^{1/\beta(ref)}}{\alpha(x)^{1/\beta(x)}} , \qquad (6)$$

where y_{std} is equal to CIBR or N/W value evaluated for standard conditions.

The results of our sensitivity analyses are described below and summarized in Table 1.

Effect of background reflectance

Vegetation

As shown in Figure 3, vegetation (here alfalfa) presents a water absorption feature centered near 950 nm. The presence of such bands *in the* surface reflectance violates the reference model condition of constant (gray) reflectance. The fractional changes introduced in the retrieved atmospheric water amount by the presence of vegetation water is shown in Figure 4a. For both CIBR and N/W algorithms, the water amount derived from the constant reflectance law is greater than that derived from the altered law by up to 8% for CIBR and 14% for N/W, depending on the total water abundance present. This result indicates that over a collection of vegetated and unvegetated areas, the latter having 25% reflectance independent of wavelength, and both under uniform atmospheric moisture distribution, an apparent variation in water vapor would be found employing these simple algorithms, with higher values over the vegetated areas. N/W proves to be slightly more sensitive to vegetation background reflectance than CIBR. Frouin and Middleton (1990) did simulations with the 5S radiative transfer code (Tanré et al., 1985) *utilizing* a wide range of surface materials, including rocks, minerals, soils, and wet and dry vegetation. They found on average that the scatter in retrieved

atmospheric water abundance was reduced by a factor of three with the N/W technique, but the specific case of vegetation was not isolated. On a large areally averaged basis including many soil, rock and vegetation types, the N/W method should yield more accurate results. On a pixel by pixel basis at scales typical of AVI RIS imagery, individual spectral types become important and need to be accounted for.

Soil containing gypsum

Hydroxyl minerals such as gypsum present a water absorption feature around 960 nm (Figure 3) similar to that in vegetation. The assumption of a constant background reflectance where gypsum (or any other hydroxyl mineral) is present in the surface mineralogy introduces an overestimation of the amount of water retrieved by up to 10% for CIBR and 15% for N/V/ (Figure 4b, Table 1). As for vegetation, in the spectral interval occupied by the atmospheric water band, the reflectance is a non-linear function of wavelength. The surface reflectance effect does not cancel out in construction of the N/W or CIBR law. CIBR is again less sensitive than N/W.

Soil containing Iron oxides

Soil including iron oxides (Figure 3) presents a broad absorption feature extending from 780 to 1300 nm. In the spectral interval occupied by the atmospheric water band, the reflectance is approximately a linear function of wavelength. The surface reflectance effect averaged over the N/M/ law spectral intervals thus tends to cancel out in construction of the N/W law, whereas it does not for CIBR. The result is clearly shown on Figure 4c where N/M/ overestimates the water by only 2% compared to uniform conditions versus 10'% for CIBR.

General variation of the average reflectance from the standard value

The previous analyses dealt with the effects on CIBR and N/W retrievals of a composite reflectance variation consisting of: (1) a spectrally varying part arising from an absorption band, end (2) a spectrally gray component. The average reflectance near 940 nm for the materials examined also undergoes large changes from the model assumed value of 25% as follows: iron oxides (19.8Ye), alfalfa (63.8%), and gypsum (68.8%). In the present section, we evaluate systematic error resulting from changes in the spectrally gray reflectance away from an assumed standard gray *value.* That is, if a calibration law is developed for an assumed reflectance R_s, variations away from R_s will give rise to unreal variations in the retrieved water vapor in an otherwise uniform atmosphere. Two cases are considered here: (1) small departure (on the order of 1 %) from an average gray reflectance; this accounts for small lateral changes in reflectance over homogeneous areas in AVIRIS images; (2) gross departure from the reference gray reflectance Of 25%, reflecting lateral changes in reflectance expected over heterogeneous AVIRIS scenes.

In the first case, the reflectance range investigated was subdivided into two parts as follows: (1) $0 \leq R \leq .05$, and $.05 \leq R \leq .70$. The first interval pertains to water vapor analyses at 940 nm over dark targets, particularly standing water bodies, while the second is applicable to most land surfaces (rocks, soils, vegetation, snow, and ice). The fractional change in retrieved water amount $\Delta W/W$ accompanying a small change A_R in the background reflectance away from an assumed standard reflectance R_s is given approximately by

$$\frac{\Delta W}{W} = \frac{\Delta R}{R} \left(\frac{\partial y_{c,f}}{\partial R} \right)_{W,V} / \left(\frac{\partial y_{c,f}}{\partial W} \right)_{R,V} \qquad (7)$$

where yc,f indicates either the CIBR or N/W form of Equation (2).

These changes for a one percent variation of A_R of R are plotted in Figure 4d and 4e for seven values of reflectance in the range $.01 \leq R_S \leq .60$ (the changes for $.60 < R_s \leq .70$ were too small to show). Vulnerability of the CIBR and N/W retrievals to background reflectance variations (constant in wavelength) is high for R_s near zero; errors of this type however decrease rapidly with increasing reflectance to negligible magnitude at R_S = .60.

In the case of gross departures from the average reference reflectance (25%), the fractional systematic error as described in Equation (6) was evaluated for three surface reflectance (R = 0.10, 0.20, and 0.50). In every case (Figure 4f), the N/W technique shows to be more sensitive than CIBR, the highest errors been observed for $R \leq 0.25$. The amount of water retrieved is underestimated by up to 20?6 for CIBR and 22% for NM/ while it is overestimated by up to 7% for both techniques when R >0.25.

Difference attributable to spectral variation of the surface reflectance

As mentioned previously, departures from the reference reflectance are a combination of two phenomena: a change in the gray component (see above) and a spectrally varying part arising from an absorption band. In this section, we attempt to characterize the fractional changes $A\ W/W \approx (W_c - W_i)/W_c$ that only results from the absorption features or slope in reflectance over the 870 - 1040 nm range, where the subscript c designates constant reflectance (63.8% for alfalfa for example) and i the wavelength dependent reflectance of the mineral species or vegetation. Using Equation (3)

$$\frac{\Delta W}{W} \approx \frac{1}{\beta_c}\left(\frac{\Delta\alpha}{\alpha_c}\right) + \ln(W)\left(\frac{\Delta\beta}{\beta_c}\right) \quad . \qquad (8)$$

These differences for a soil containing iron oxides, alfalfa and a soil containing gypsum are shown in Figure 4g. As observed for the previous cases, errors in water retrieved are higher for N/W than CIBR. Additionally, the two techniques present different behaviors. The presence of an absorption feature centered around 950 nm (vegetation, gypsum, etc.) has very little effect on the CIBR recoveries if the average (gray) reflectance is known (underestimation by about 5%). in the case of linear spectral variations (iron oxides for example), the error is more important (overestimation by up to 8%). For N/W, the magnitude of errors is important (overestimation by 25 to 30%) and is independent of the linearity of the reflectance variation introduced by the absorption over the wavelength range considered.

Effect of Meteorological Range

In the LOWTRAN 7 model, atmospheric turbidity is parameterized by surface meteorological range (V), which is computed from Koshmieder's formula (Kneizys et al., 1988) using atmospheric extinction due to scattering at 550 nm. Atmospheric extinction properties can be accurately estimated when sunphotometer measurements are made concurrently with AVIRIS overflights. They allow retrieval of the aerosol optical depth along the iine of sight to the sun as a function of time (Bruegge et ai., 1992 and references therein). But they can oniy be made at specific places in the ground track along the line of sight, from the observing point to the sun. In general, the variations of aerosol loading from place to place are not known, nor are estimates of extinction obtainable from the AVIRIS data themselves, except when values of surface spectral reflectance may be available. Thus, it is important to estimate the sensitivity of the

retrieved water abundances to aerosol variability. Both vertical and horizontal variability may be important. The vertical structure aerosol models present in LOWTRAN 7 are described by Kneizys et al. (1988), Sec. 6. In the present section, we evaluate the gross systematic errors that result from an assumed horizontal variability of V. The vertical aerosol structure (Case 4 of Kneizys et al., 1988) is assumed invariant.

Gross departure of V from the value assumed in construction of the reference calibration law (e. g., 25 km) leads to systematic errors in water vapor measured that are given in Figure 5. Encountering visibility conditions of 5 km leads to an overestimation of. water retrieved relative to the reference state by about 300/. for both CIBR and N/W algorithms (Figure 5a), with errors increasing sharply as the column moisture abundance approaches zero. With V = 50 km (Figure 5b), the amount of water is underestimated by up to 10 - 20% for CIBR. For N/W, the amount is underestimated by up to 5% for water amounts lower than 2 cm and overestimated by up to 4% when the water amount is higher than 2 cm. At V = 100 km (Figure 5c), the water retrieved is underestimated by up to 30% for both CIBR and N/W. In the extreme case of V = 250 km (Figure 5d), corresponding to essentially clear atmospheric conditions relative to standard value of V, the amount of water retrieved is underestimated by up to 40% for both CIBR and NAN.

if the actual water vapor distribution in the atmosphere is uniform, but the aerosols are variable in abundance from place to place (lateral changes), then an apparent but unreal variation in the retrieved water vapor amounts will be observed. The perturbation in retrieved water abundance Δw resulting from a perturbation ΔV away from the standard state is given approximately by

$$\Delta W_{c,f} \approx \left(\frac{\partial y_{c,f}}{\partial V}\right)_W \Big/ \left(\frac{\partial y_{c,f}}{\partial W}\right)_V \Delta V \,. \qquad (9)$$

The fractional change in water abundance $\Delta W_{c,f}/W$ for various values of ΔV are shown as a function of W in Figure 6. For both techniques, positive ΔV lead to lower apparent values of W compared to the uniform abundance (amount retrieved underestimated by up to 6%). Such perturbations rapidly become less important with increasing V.

Effect of aerosol type

LOWTRAN 7 provides 26 wavelengthdependent aerosol scattering phase functions (Kneizys et al., 1988). To illustrate the dependence of retrieval errors on the choice of such models, we intercompared three of the standard types, rural, urban, and maritime. The reference model is that of rural aerosols. All three models together with particle size distributions are described by Shettle and Fenn (1979). The angular scattering properties are summarized in Kneizys et ai. (1 988, Appendix D). Seventy phase functions are contained in LOWTRAN 7. The rural aerosols are assumed there to be comprised of 70% water-soluble material (ammonium and calcium sulfate and organics) and 30% dust aerosol. Urban aerosols contain a rural aerosol background modified primarily by addition of a sooty carbonaceous component. The maritime aerosol model has a sea-salt component from evaporation of sea spray and represents reaggregation of water to sait nucleae under high relative humidity conditions.

At V = 25 km, the assumption of a rural aerosol for the reference state and its use where marine aerosol conditions prevail leads to an overestimation of water for low moisture conditions (W c 1 cm) of a few percent for both CIBR and N/W algorithms (Figure 7a). For moister conditions (W > 1 *cm)* the water present is underestimated by 3 to 4?40.

In the presence of urban aerosols, employing a standard model leads to underestimates of water as great as 10 -15% for a dry atmosphere (Figure 7b).

Vertical distribution of aerosols can also affect water recoveries. This case is fairly complex to implement in LOWTRAN 7 and has not been considered here.

Viewing and Illumination effects with anisotropic aerosol scattering

In water retrieval problems with AVIRIS, aerosol scattering has sometimes been neglected (Gao and Goetz, 199o). Further, to ease the burden of calculation, retrievals with LOWTRAN 7 have sometimes been carried out assuming uniform nadir viewing across an image track, and, in addition, an AVIRIS flight azimuth of NO (flying towards North) regardless of the actual image path orientation (Carrère et al., 1990; Green et al., 1990a). These assumptions discount the effects of anisotropic aerosol scattering as well as variations in the slant path attenuation from side to side of the image swath. The purpose here is to estimate the magnitude of the errors introduced by neglect of these geometric factors.

For anisotropic scattering, the radiance emergent from the atmosphere at AVIRIS depends upon the angular properties of the phase function, and the scattering phase angle. There are additional factors describing illumination and view angle factors and slant path attenuation.

AVIRIS views the surface at angles of $\pm$ 15° about nadir across the image track. The positive sign corresponds to the portion of image line at an angle of $\pi/2$ to the flight direction, and the negative sign to an angle of $3\pi/2$. There is a corresponding variation of the scattering phase angle Θ across an AVIRIS scene given by Θ_1 (positive side) and Θ_2 (negative side) where

$$\text{Cos}\ \Theta_1 = -\left[\sin\theta \sin\varphi \sin\theta_0 + \cos\theta \cos\theta_0\right] \qquad \text{(lo)}$$

and

$$\cos \Theta_2 = \sin \theta \sin \varphi \cos \theta_0 - \cos \theta \sin e. . \qquad (11)$$

In Equations (10) and (11), θ is the angle between the nadir direction and line of sight from a point on the ground to the instrument along an image line (varies ± 15% with sign convention as previously described). As shown on Figure 8, the relative azimuth angle φ is equal to $\pi - \varphi_0 + \varphi_{AV}$, where φ_0 is the azimuth angle Of the sun, and φ_{AV} is the azimuth of the AVIRIS flight direction both measured positive clockwise from north. As before, θ_0 is the solar zenith angle. The azimuth angle ψ for the positive across track direction (this direction corresponding to the atmospheric path from sensor to surface) is simply given by $\psi = \varphi_{AV} + \pi/2$. For the reference conditions (nadir looking, flying towards north, i. e., θ = O and φ_{AV} = O), the scattering phase angle is independent of φ; the azimuth of the sun φ_0 is 159.20; the solar zenith angle θ_0 is 26.4°. Under these conditions, the scattering phase angles Θ_1 and Θ_2 at $\theta = \pm$ 15° vary with φ between approximately 140° and 170°. Θ_1, for example, reaches a maximum at $\varphi = \pi/2$ and a minimum at $\varphi = 3\pi/2$, while Θ_2 is a minimum at $\varphi = \pi/2$ and a maximum at $3\pi/2$. The phase functions employed (see Kneizys et al., 1988, Appendix C) reach maximum values at Θ = 1700 and the minimum value at 140°. At these phase angles, the path radiance scattered to the sensor is a maximum or a minimum respectively. Calibration relationships like Equation (3) were developed for angular increments $\Delta\psi$ of 45° for O ≤ ψ s 360°. Figure 9 illustrates the fractional variation in water vapor retrieved for θ = ± 15° as a function of path azimuth angle ψ as derived from these LOWTRAN 7 simulations. CIBR and N/W are affected in a similar manner. The maximum error occurs for $\psi = \pi/2$, with water amount being underestimated by up to 3%, and the minimum for $\psi = 3\pi/2$, with an underestimation less than 0.5%.

SYSTEMATIC AND RANDOM ERRORS FROM INSTRUMENTAL CAUSES

Changes In radiometric calibration coefficients inflight

The AVIRIS laboratory and inflight radiometric calibrations supply relationships between instrument response ($DN(\lambda_i)$) and incident radiance ($L(\lambda_i)$) at the i-th channel of the form

$$DN_i(\lambda_i) = \frac{L(\lambda_i)}{\Phi(\lambda_i)} + DN_0(\lambda_i) \qquad (i = 1,..,224) \qquad (12)$$

where the $\Phi(\lambda_i)$ are the radiometric calibration coefficients and the $DN_0(\lambda_i)$ are dark current instrument responses. Laboratory calibration coefficients are commonly used to convert AVIRIS measured DN in flight to radiance. Their validity is checked through field calibration experiments at the beginning and end of each flight season. Any change in instrument behavior inflight during the course of the season, such as variation of channel wavelength assignments λ_i or widths of the channel response functions away from laboratory determined values (which would suggest optical defocusing or distortion of the dispersed radiation on the detector arrays), electronic problems such as drift in the offset or signal loss, induces a change in the coefficients $\Phi(\lambda_i)$. The change $\Delta L(\lambda_i)$ implied by a change $\Delta\phi(\lambda_i)$ in the calibration coefficients inflight is

$$\frac{\Delta L(\lambda_i)}{L(\lambda_i)} \approx -\frac{\Delta\Phi(\lambda_i)}{\Phi(\lambda_i)} \qquad (13)$$

The magnitude of the error in amount of water retrieved using the CIBR or the N/W approach will depend on the magnitude of the $\Delta L(\lambda_i)$ so introduced, which will vary with

λ_i. As such, magnitude of error is difficult to assess in a sensitivity analysis. The cases of changes in channel wavelength positions and channel width are presented below. A tentative estimate for other possible sources is made further in this paper when applying the techniques to AVIRIS data over Salton Sea.

Effect of in-fllght change In AVIRIS channel positions

Shifts up to 1 nm in AVIRIS in-flight channel positions have been observed during calibration experiments (Green et al., 1990b). An assessment of the effect of shifts in channel positions on the amount of water retrieved was performed for a range of ±1.0 nm from the provided channel position file established by a laboratory calibration of AVIRIS (Green et al., 1990b). Figures 10a and b show that the CIBR and N/W respond differently to these shifts. The retrieval error increases regularly and symmetrically for the CIBR (overestimation by up to 6'% for positive shift, i.e., a shift in channel position towards longer wavelength; underestimation by up to 9% for negative shift). The worst case is very small shifts (± 0.1 nm) for the N/W approach, leading to an overestimation up to 6°/0, with no systematic dependence on the sense of shift.

Effect of in-flight change In AVIRIS channel width

Increasing widths of the channel response functions up to +1.9 nm (extreme case of 5.9 nm) have been 'reported during calibration experiments (Green et al., 1990b). The effects of in-flight change of AVIRIS response functions on water retrieval are shown on Figure 10c and d. The error from this source increases" regularly for CIBR but stays very small (maximum of ±1%). N/W is more greatly affected by these changes, the worst being for a narrowing of channel width which leads to an overestimation of up to 6.8%.

Minimum detectable limits of water vapor variation given AVIRIS Noise-Equivalent Radiance

The noise in AVIRIS data is estimated in the laboratory calibration from end of image line dark current instrument response (Chrien et al., 1990), and inflight by the same procedure or by examining the variance of signals received from uniform calibration targets (Green et ai., 1990b). The noise-equivalent radiance (NER) is calculated by applying the laboratory determined radiometric calibration coefficients. All such methods yield consistent NER estimates. In the 940 nm region, the current value of the NER is about 0.06 $\mu W/cm^2/nm/sr$ (Green et al., 1990 b). The NER determines the precision of water vapor retrieval using either of the algorithms employed here. Application of classical error propagation formulas (Bevington, 1969, chap. 4) to the calibration laws (Equation (2) and (4)), neglecting the correlations between band radiances, yields the following equations for determination of the fractional random error in water abundance $(\sigma_W/W)_{CIBR}$ and $(\sigma_W/W)_{N/W}$ in terms of the observed radiances L_j and the NER denoted as σ_L,

$$\left(\frac{\sigma_w}{W}\right)_{CIBR} = \left(a_c\, b_c\, W^{b_c}\right)^{-1} \sqrt{+\,2\,\frac{L^2}{(C_1 \quad + C_2)^2}}\,\left(\frac{\sigma_L}{L}\right) \qquad (14)$$

and

$$\left(\frac{\sigma w}{W}\right)_{N/W} = \sigma_L \left(a_f\, b_f \quad W^{b_f}\right)^{-1} \sqrt{\frac{3}{L_n^2} + \frac{7}{L_W^2} - \frac{6}{L_n L_W}} \quad " \qquad (15)$$

The constants a_c, b_c and a_f, b_f pertain to CIBR and N/W respectively and $n = L_3 + L_4 + L_5$, $m = L_1 + \ldots + L_7$. To estimate the fractional errors, we simulated the radiances L_j for the 940 nm water band as a function of W using LOWTRAN 7 for the reference. These

results are given in Figure 11a. The minimum detectable differences in water vapor column abundance σ_w as a function of W are given in Figure 1 lb.

APPLICATION TO AVIRIS DATA

The Salton Sea test site

The Salton Sea area is located in the Salton Trough of southeastern California, approximately 240 km ESE of Los Angeles. The water body is 1100 km^2 in area with a present surface elevation of about -70 m and a maximum depth of 15 m. The average salinity of the Sea is about 44,000 ppm or 1.26 that of the ocean water. Land areas west and east of Salton Sea consist of bahadas covered with sparse desert scrub vegetation and rugged mountain ranges that are devoid of vegetative cover. Algodones Dunes, 60 km southeast of the southern lake shore, is a large accumulation of sand. Imperial Valley, immediately to the southeast, is a topographically flat area of intense agricultural activity in large checkerboard tracts of cultivated and fallow ground adjacent to one another (Figure 12). Both farmed and fallow areas adjoin free-standing water in the Sea itself. The area is characterized by high humidity. Some areal variability in atmospheric moisture was expected from evapotranspiration, advected moisture accompanying sea breezes, and evaporation from cooling towers of scattered geothermal power plants. The small variation in surface elevation over land areas (few meters near the southeastern shore) minimized variations in water vapor from place to place due to topographic effects.

AVIRIS observations at Salton Sea

AVIRIS overflew the Salton Sea test site on October 3, 1990, under clear skies, between approximately 11:40 a.m and 1:00 p.m Pacific Standard Time. Data were acquired along three flight lines (Figure 13): (1) the first was obtained with AVIRIS flying N140; (2) for both the second and third lines, AVIRIS headed N35. These lines overlapped with a common area approximately 11 x 11 km square, proximate to the southern shore of the Sea.

Field measurements

During the morning of the overflight and throughout the overflight periods themselves, atmospheric extinction and water vapor column abundances were measured at Salton Sea National Wildlife Refuge (SSNWR, Figure 13) using a Reagan sunphotometer (Reagan et al., 1987). The Reagan sunphotometer provides solar radiance measurements for 10 spectral channels (370, 400, 440, 520, 670, 780, 870, 1030 nm; 610 nm for ozone and 940 nm for water vapor) in 10 nm bandpasses. Methods of deriving spectral aerosol optical depths via the Langley technique and the time-dependent water vapor path abundances, including compensation for aerosol extinction at 94o nm, are described in detail in Reagan et al. (1987) and Bruegge et al. (1990, 1992). The time-dependent water vapor column abundance measured is shown in Figure 14a.

Implementation of the CIBR and N/W algorithms at Salton Sea

A value of 332 km was first estimated, using the Reagan observations, from the total atmospheric extinction at 560 nm using the least square slope of the Langley plot. To

secure agreement between the optical depth derived from the Reagan measurements and the optical depths used in LOWTRAN 7 (derived from the one-way vertical transmittance), particularly between 870 and 1030 nm, V had to be decreased to 190 km (Figure 14b). This value of V was subsequently used in the LOWTRAN 7 code to develop CIBR and N/W water calibration laws for the Salton Sea images. In addition, we assumed a LOWTRAN model ground spectral reflectance equal 25%, independent of wavelength, nadir viewing, and a rural aerosol scattering model with standard vertical distributions of both water vapor and scatterers specific to the midlatitude summer model.

Evaluation of errors from random and coherent instrument noise for inflight conditions

Uncertainty limits from random plus coherent noise present in the AVIRIS data for the three Salton Sea overflights shown on Figure 14b were estimated for inflight conditions from error propagation formulas given by Bevington (1969) and appiied to the CIBR and N/W retrieval algorithms as defined in Equations (2), (3), and (4). The present evacuations include both variances and covariances of the inflight band radiances, whereas the analysis of minimum detectable limits of water vapor variation described earlier was restricted to inclusion of the variances alone (Equations (14) and (15)). In the previous analysis, variances of the band radiances were taken to be uniform with wavelength and equal in magnitude to the (square) of the NER obtained from the laboratory calibration. For inflight conditions, the covariance matrices of band radiances for both algorithms were obtained from a 50 x 50 pixei offshore area of the Salton Sea to help minimize influences of sediment turbidity in the water and consequently non-zero surface reflectance. These estimates of the variance contain contributions both from the surface reflectance of water over the sampie area and the

atmosphere, in addition to instrumental fluctuations. Both the surface and atmospheric contributions were expected to provide additional sources of variation in the inflight noise estimates. The matrices of radiances derived from the variance-covariance noise matrices σ_{ij} for CIBR and N/W bands are

$$[\sigma_{ij}^{1/2}]_{CIBR} = \begin{matrix} 0.0551 & & \\ 0.0212 & 0.0291 & \\ 0.0309 & 0.0174 & 0.0330 \end{matrix} \qquad (16)$$

and

$$[\sigma_{ij}^{1/2}]_{N/W} = \begin{matrix} 0.0376 & & & & & & \\ 0.0132 & 0.0319 & & & & & \\ 0.0185 & 0.0888 & 0.0291 & & & & \\ 0.0156 & 0.0112 & 0.0145 & 0.0311 & & & \\ 0.0209 & 0.0899 & 0.0150 & 0.0139 & 0.0316 & & \\ 0.0214 & 0.0121 & 0.0166 & 0.0154 & 0.0173 & 0.0301 & \\ 0.0232 & 0.0829 & 0.0147 & 0.0118 & 0.0185 & 0.0189 & 0.0302 \end{matrix} \qquad (17)$$

where the square root symbol means application to each matrix element individually.

The spectral variation of the NER as estimated by from the laboratory dark current observations (averages of 101 image lines per spectral band) and the inflight dark current values (averages of 50 image lines per spectral band), both converted to equivalent radiance using the laboratory spectral radiometric calibration coefficients, are compared to the spectral NER estimates based on the covariance analysis in Figure 15. The analysis based on the variance-covariance matrix yields an estimate of NER comparable to that provided by the end-of-line dark current from both the inflight and laboratory measurements. Contributions to the observed variances by surface and atmospheric sources are evidently negligible.

The previous formulas Equations (14) and (15) have been modified to include the covariance contributions to the fractional uncertainties to σ_y/y of the two calibration laws and hence to σ_W/W. For example, the additional terms for σ_y with CIBR are

$$\sigma^2_{y_c} = y_c^2 \frac{\sigma^2_{12}}{2\,L^2_{avg}} - y_c \frac{\sigma^2_{13}}{L^2_{avg}} - 2y_c \frac{\sigma^2_{23}}{L_{avg}} \cdot \qquad (18)$$

A similar much lengthier formula obtains for the N/W algorithms. In Equation (18) the presence of minus signs on the second and third terms combined with all positive values of the CIBR σ_{ij} (in the present estimate of this matrix) actually contribute to a reduction of the corresponding formal uncertainty in W of about 16%.

Analysis of spatial distribution of water vapor on AVIRIS images using reference conditions

Reference conditions (nadir viewing, R = 0.25, V = 190 km, rural aerosols) were used to create images *of* spatial distribution of water vapor over the Salton Sea area from AVIRIS data using the CIBR and N/W techniques. Results are shown in Figure 16.

Three observations can be made from these images: (1) the amounts of water retrieved by the two techniques are different, N/W recovering 4 to 5 mm more than CIBR; (2) the contrast between green fields and fallow areas (as determined from Figure 12) is sharper on the N/W image, confirming results from the error analysis which predicted a higher overestimation of water over vegetated areas for N/W when using a constant gray reflectance of 25% in the model. As shown on Figure 17, which illustrates the relationship between the Normalized Difference Vegetation Index (NDVI), a classical index used to detect green vegetation, and the amount of water retrieved from the AVIRIS radiance data using the two techniques, the magnitude of the overestimation matches what was expected, around 60/0 for CIBR and 13% for N/W; (3) the amount of water retrieved

changes through time. Water is maximum over green fields for flight#2, around 12 neon 100al time. The average water amount drops for the third flight, around 1 pm local time. Such observations could be related to evapotranspiration over vegetated areas and change in sea breeze direction. Unfortunately no ground observations were available in vegetated areas at the time of the flight. The nearest evapotranspiration estimate available was made in Calipatria, a couple of miles East of the area covered by the AVIRIS flights. This data set shows a maximum for evapotranspiration between 12:30 and 1:30 pm 100al time.

Since the only ground observation available were made at the SSWNR, in a bare field, next to a building, an attempt was made to validate the AVIRIS retrievals by adjusting model parameters to ground conditions and comparing with the water retrieved from the Reagan sunphotometer observations.

Validation at the SSNWR site

Validation was performed by comparison between ground observed and AVIRIS retrieved water amount after adjustments of the model parameters to site conditions. Parameters needing to be adjusted were: (1) viewing geometry; (2) background average reflectance; and (3) type of aerosol. As shown on Figure 13, the SSNWR is boated close to the edge of the flight lines. Viewing geometry has to be adjusted to take into account the variation in radiance with phase angle due to anisotropic aerosol scattering and slant path attenuation at the edge of the flight line. Area corresponding to the site was viewed by AVIRIS 140 off-nadir for flight#l, and 120 off-nadir for flight#2 and 3.

In a second step, an estimate of the ground Lambertian reflectance R at 940 nm relevant to the 5x5 pixel area used in the analysis was obtained by averaging the reflectance implied by the AVIRIS radiances at 882 and 997 nm (where atmospheric

transmittance is high and absorption, due to atmospheric gasses is minimal) using the relationship

$$R = \pi L_{AVIRIS} / \left(E_0 T^2 \cos \theta_0\right) . \qquad (19)$$

In Equation (19), E. is the solar spectral irradiance, T the one-way vertical transmittance of the atmosphere determined from LOWTRAN 7. The relevant data for these evaluations are given in Table 2. The slight 'differences in retrieved reflectance for the three flights can be explained by the use of a 5x5 pixel area and some inaccuracy in locating the site on the images. In a third step, an adjustment was made for aerosol type, based on the proximity of the Salton Sea. As mentioned above, Salton Sea is a large saline water body contributing substantial atmospheric moisture over the water body and adjacent land areas. Actual aerosols properties at the time of the AVIRIS overflights are unknown. The standard marine aerosol model resident in the LOWTRAN 7 code was used as perhaps the closest approximation to hydrose aerosols easily available to us.

Retrieved amounts of water for the three AVIRIS overflights after adjustment of model parameters are shown on Figure 18. Change from rural to marine aerosols did not make much of a difference because of the high visibility (V = 190 km) at the time of the flights.

However, these adjustments did not decrease the discrepancy between N/W and CIBR recoveries. A detaiied analysis comparing AVIRIS and LOWTRAN 7 modeied radiance for the SSNWR site was performed in order to understand the cause of this discrepancy. The case of the first AVIRIS flight is presented in the following section.

Reconciliation of differences between CIBR and N/W retrievals based on model assumptions and AVIRIS radiometry

We will explore here a numerical reconciliation of the differences between the CIBR and N/W retrievals for the Salton Sea data set based on differences in the radiances supplied by AVIRIS and those generated by LOWTRAN 7 for the observing conditions. We have assumed that: (1) the water column abundance generated from the Reagan sunphotometer is accurate, and (2) that the entire burden of disagreement between CIBR and N/W water values shown on Figure 18 resides in differences between LOWTRAN 7 and AVIRIS radiances L_j present in the algorithms. This latter assumption means that the altered values L_j' are assumed given by $L_j + \Delta L_j$ where ΔL_j may vary from band to band. Specifically, the ΔL_j are taken equal to $L_{j,LOWTRAN} - L_{j,AVIRIS}$, where $L_{j,x}$ represents the radiance in band j supplied by either LOWTRAN 7 or AVIRIS for the particular geometry of the AVIRIS observations with respect to the ground observing station (as described above). LOWTRAN 7 was further constrained using the water vapor abundance retrieved from the Reagan sunphotometer data for the time of overflight (2.79 cm). Resulting radiances for the SSNWR site are shown in Figure 19. Using the CIBR algorithm as an example, the difference ΔL_j depicted on Figure 19 generates a difference Δy_{CIBR} given approximately by

$$\Delta y_{CIBR} \approx -\left[\Delta L\left(-\frac{\Delta C_1}{2L_{avg}^2} + \frac{1}{L_{avg}} + \Delta C_2\left(\frac{\Delta C_1}{2L_{avg}^3} - \frac{1}{L_{avg}^2}\right)\right)\right] \quad (20)$$
$$+ \Delta C_1 \frac{L}{2L_{avg}^2} - \Delta C_2 \left(\frac{\Delta C_1}{2} \frac{L}{L_{avg}^3} - \frac{L}{2L_{avg}^2}\right)$$

(a similar much lengthier formula obtains for the differences $\Delta y_{N/W}$). Using Equation (18), this leads to a fractional water difference $\Delta W/W$ of +.13, i. e., the water vapor

amount derived from the CIBR calibration law using the AVIRIS observed radiances is 13% less than that assumed in the theoretical model. The corresponding value for the N/W algorithm is -.03, so that the derived water abundance is 3% greater than that used in the model. Comparable differences were found for the other Salton Sea overpasses. Observed discrepancies after final adjustments (Figure 19) were on the order of 13% for CIBR and O to 2% for N/W. A detailed accounting of the individual band-by-band differences between AVIRIS observed and LOWTRAN 7-derived radiances thus accounts for both sense and magnitude of the difference found between the water vapor abundances retrieved with each algorithm. The N/W algorithm is much less sensitive to fluctuations of this type. The present analysis does not indicate sources of the detailed radiance differences observed. These might equally well originate in the instrument, the atmosphere, through (unknown) wavelength variations of the surface spectral reflectance, or from LOWTRAN 7 itself. This emphasizes the extreme sensitivity of the 3-point CIBR technique to any difference in radiance which could be an advantage (better accuracy in the retrieval) if both instrument and model predicted radiances were well characterized.

CONCLUSIONS

Two simple techniques (CIBR and NAN) to retrieve path precipitable water from imaging spectrometer radiance data using the 940 nm water absorption band were compared. Analysis of systematic and random errors based on the radiative transfer code LOWTRAN 7 showed that the 3-point CIBR approach was less sensitive to systematic errors from calibration model assumptions (April 18, 11:05 PST, Latitude = 33.2N, Longitude = 115.5W, R = 0.25, V = 25 km, rural aerosols, nadir viewing, flying north) except for change in meteorological range. Small departure from the model average reflectance over dark targets (0.01 c R < 0.05) such as standing water bodies, and gross

departure from model meteorological range (V = 25 km) had the most critical impact on the accuracy of water retrievals. A 1% change in reflectance from the model value lead to an overestimation of the water retrieved by more that 30%. Assuming 25 km visibility when V = 5 km lead to overestimation of 35% and underestimation of 25 to 30% when V ≥ 100 km.

The N/W approach proved to be highly sensitive to changes in reflectance solely due to absorption features, the average gray reflectance being known. Water amount retrieved could be overestimated by more than 28%.

Both techniques were then applied, using reference conditions (R = 0.25, V = 190 km, nadir viewing, rural aerosols) to three AVIRIS flights over Salton Sea. As predicted by the sensitivity analysis, the amount of water retrieved over vegetated areas was higher for N/M/ than for CIBR. Changes through time were observed, possibly due to evapotranspiration and change in sea breeze pattern, but could not be validated.

Validation was performed by comparison with in-situ observations at the SSNWR. After adjustment of model parameters for the site, N/W showed closest match with observed data. The discrepancy between observed, N/W-retrieved, and CIBR-retrieved water abundances could be explained by small band to band differences between modeled and observed radiances. The radiance differences may equally well originate in the instrument, the atmosphere, through unknown wavelength variation of surface spectral reflectance or from LOWTRAN 7 itself. This emphasizes the importance of accurate instrument calibration inflight and accuracy of absorption model for water to minimize errors.

A similar analysis using the radiative transfer code MODTRAN (Berk et al., 1989), which presumably has a better water absorption model and higher spectral resolution will be performed to address this issue. This analysis will also include the unsaturated 1130 nm water absorption band which should be less sensitive to changes in aerosol type and distribution as well as scattering. Plans are also to apply both techniques to

more recent AVIRIS data with concurrent ground measurements (ground reflectance, optical depth, water vapor, E.T., wind speed and direction) at various sites on the image, more specifically bare soil and vegetated areas, to better understand water distribution patterns, their evolution through time, and their link with AVIRIS retrieved values.

Acknowledgements

The authors would like to thank Carol Bruegge for reducing the Reagan data, and two anonymous reviewers for their comments. J.C. wishes to acknowledge J. van den Bosch for her help with some of the calculations, and G. Hoover for helpful discussions. This work has been carried out at the Jet Propulsion Laboratory, California Institute of Technology in relation to the HIRIS Project, under a contract with the National Aeronautics and Space Administration.

References.

Berk A., Bernstein L. S., and Robertson D.C. (1989), *MODTRAN: a Moderate Resolution Model for LOWTRAN* 7. AFGL-TR-89-01 22, Air Force Geophysics Laboratory, Hanscom AFB, MA 01731 (April 1989).

Bevington P.R. (1969), *Data reduction and error analysis for the physical sciences,* McGraw-l-fills Book Company, New York.

Bruegge C.J., Conel J. E., Margolis J. S., Green R. O., Toon G., Carrère V., Holm R. G., and Hoover G. (1990), In-situ atmospheric water-vapor retrieval in support of AVIRIS validation. *SPIE,* vol.1298, Imaging Spectroscopy of the Terrestrial Environment, p.150-163.

Bruegge C. J., Danielson E. D., Martonchick J. V., Conel J. E., and Diner D. J. (1992), Aerosol optical depth mapping of the Konza Prairie during FIFE. *J. Geoph. Res.,* (in press).

Carrère V., Conel J. E., Green R. O., Bruegge C.J., Margolis J. S., and Alley R.E. (1990), Analysis of atmospheric water vapor maps from AVIRIS at Salton Sea, California: Part I, Experiments, Methods, Results, and Error Budgets. *Proceedings of the Second Airborne Visible/Infrared Spectrometer (A V/R/S) Workshop,* June 4 and 5, 1990, JPL Publication 90-54, p.1 07-128.

Chrien T., Green R. O., and Eastwood M.L. (1990), Accuracy of the spectral and radiometric laboratory calibration of the Airborne Visibie/infrared Imaging

Spectrometer (AVIRIS). *Proceedings of the Second Airborne Visibie/infrared Spectrometer (AVIRIS) Workshop,* June 4 and 5, 1990, JPL Publication 90-54, p.l-14.

Conel J. E., and Carrère V. (1990), Analysis of atmospheric water vapor maps from AVIRIS at Salton Sea, California: Part II, Surface moisture flux, boundary conditions, and plume measurements. *Proceedings of the Second Airborne Visible/Infrared Spectrometer (AVIRIS) Workshop,* June 4 and 5, 1990, JPL Publication 90-54, p.129-148.

Fowle F.E. (1912), The spectroscopic determination of aqueous vapor. *Astrophys. J., 35,* p.149-153.

Fowle F.E. (1913), The determination of aqueous vapor above Mount Wilson. *Astrophys. J., 37,* p.359-372.

Frouin R., and Middleton E. (1990), A differential Absorption Technique to estimate atmospheric total water vapor amounts. *Proceedings of Amen'can Meteorological Society Symposium on the First ISLSCP Field Experiment (FIFE),* Feb. 7-9, 1990, Anaheim, California, p.135-139.

Frouin R., Deschamps P.Y., and Lecomte P. (1990), Determination from space of atmospheric total water amounts by differential absorption near 94o nm: Theory and Airborne verification. *Journal Appl. Meteo., vol. 29,* p.448-460.

Gao B.C. and Goetz A.F. (1990), Column atmospheric water vapor and vegetation liquid water retrievals from airborne imaging spectrometer data. *J. Geophys. Res.*, 95, 3549-3564.

Gates D.M. (1956), Infrared determination of precipitable water in a vertical column of the earth's atmosphere. *J. Meteor., 13,* p.369-375.

Green R. O., Carrère V., and Conel J.E. (1990a), Measurement of atmospheric water vapor using the Airborne Visibie/infrared Imaging Spectrometer. *Image Processing'89, American Society for Photogrammetry and Remote Sensing,* Sparks, Nevada, p.31-44.

Green R. O., Conel J. E., Carrère V., Bruegge C.J., Margolis J. S., Rast M., and Hoover G. (1990b), Determination of the in-flight spectral and radiometric characteristics of the Airborne Visible/Infrared Imaging Spectrometer (AVIRIS). *Proceedings of the Second Airborne Visible/Infrared Imaging Spectrometer (A VIRIS) Workshop,* June 4-5, JPL Publication 90-54, p.15-34.

Hand J.F. (1940), An instrument for the spectroscopic determination of precipitable atmospheric water vapor and its calibration. *Mon. Wea. Rev.,* 68, p.95-98.

Kneizys F.X., Shettle E. P., Abreu L.W., Chetwynd J. H., Anderson G. P., Gallery W. O., Shelby J. E.A., and Clough S.A. (1988), *"Users Guide to Lowtran".* AFGL-TR-88-01 *77,* Air Force Geophysics Laboratory, Hanscom AFB, MA 01731" (August 1988), ADA 206773.

Reagan J.A., Theme K., Herman B., and Gail R. (1987), Water vapor measurements in the 0.94 minor absorption band: calibration, measurements, and data applications. *Proceedings of IGARSS'87*, Ann Arbor, Michigan, p.63-67.

Shettle E.P. and Fenn R. W. (1979), *Models of the aerosols of the lower atmosphere and the effect of humidity variations on their optical properties. AFGL-TR-79-02* 124, Air Force Geophysics Laboratory, Hanscom AFB, MA 01731, ADA 085951.

Tanré D., Deroo C., Duhaut P., Herman M., Morcrette J.J., Perbos J., and Deschamps P.Y. (1985), Effets atmosphériques en télédétection - logiciel de simulation du signal satellitaire clans le spectre solaire, *Proc. 3rd Int. Colloquium on Spectral Signatures of Objects in Remote Sensing,* Les Arcs, France, Dec. 6-20, p.315-320.

	CIBR	N/W	"Best"
Reflectance			
Vegetation	+5 to +8%	+14%	CIBR
Gypsum	0 to +10%	+ 10 to +20%	CIBR
Fe_2O_3	+2 to +8%	+1 to +1.5%	N/W
Small dR			
R = 0.01	+2 to +5 %	+2 to +5 %	same
R = 0.03	+5 to +10'3/0	+5 to +10%	same
R = 0.05	+20 to +30%	+20 to +35%	CIBR
R = 0.10	o to +3.5%	o" to +4%	CIBR
R = 0.40	+1%	+ 1 '?/0	same
R = 0.60	<1 %	<1 '/0	same
Gross dR			
R = 0.10	"20 to -9%	-21 to -9?40	CIBR
R = 0.20	-3 to -1%	-6 to -1%	CIBR
R = 0.50	+3 to 7%	+3 to +7%	same
Absorption			
Alfalfa	-6 to +5%	+25%	CIBR
Gypsum	-5 to +5%	+23%	CIBR
Iron oxides	o to +15%	+28%	CIBR
Meteorological Range			
Gross departures			
5km	+24 to +35%	+20 to +40%	CIBR
50km	-15 to +5%	-5 to +4%	N/W
100km	-30 to -11%	-30 to -4%	N/W
250km	-25 to -10%	-25 to -5%	N/W
Small departures			
5km	-0.5 to -6%	-0.5 to -9%	CIBR
50km	O to -4%	o to -5%	CIBR
100km	O to -1 .25%	o to -1.59'0	CIBR
250km	O to -0.3%	0 to -0.35%	same
Aerosols			
Marine	-4 to -1 %	-2.8 to 0%	CIBR
Urban	-6 to 0%	-5 to o%	CIBR

Viewing and illumination geometry			
Max (y = π/2)	-2.8%	-2.9%	sam
Min (y = 3π/2)	-0.4%	-0.4%	same
λ shift			
+0.1nm	+0.6 to +0.9%	+4 to +6%	CIBR
+0.5nm	+2 to +4%	+4 to +6%	CIBR
+l. Onm	+ 60/0	+2 to +4%	N/W
-0.1nm	-0.8 to -1?4	+5.5 to +60/0	CIBR
-0.5nm	4 to -5.5?40	+4.5%	same
-1. 0nm	-8 to -12%	+5'?/0	N/W
Width			
+0.01nm	0 %	070	CIBR
+0.05nm	+0.4 to +0.5%	+5 to +6%	CIBR
+0.1nm	-0.8 to -1%	-4 to -5.5%	CIBR
-0. 01nm	-0.8 to -1%	+5 to +6%	CIBR
-0.05nm	+0.5%	+5 to +6.5%	CIBR
-0.1nm	+0.8 to 1%	+6 to +7%	CIBR

Table 1: Summary 01 errors for both techniques
+ stands for overestimation of water amount retrieved if using the "reference" calibration curve; - for underestimating

λ	E_o	T	L_{AV}	θ_o	R
Flight#1					
882	95.92	0.932	4.38	38.16	0.21
997	74.94	0.936	3.586	38.16	0.22
Flight#2					
882	95.92	0.933	4.658	37.22	0.22
997	74.94	0.931	3.803	37.22	0.23
Flight#3					
882	95.92	0.934	4.9362	36.28	0.23
997	74.94	0.932	4.0072	36.98	0.24

Table 2: Parameters used to estimate reflectance at 882 and 997 nm for the three AVIRIS overflights and resulting reflectance.

Figure captions

Figure 1: Spectral basis of the water mapping algorithms: a- The CIBR technique; CI and C_2 are continuum values, L, upwelling radiance at the wavelength of maximum absorption for water: b- The NM/ technique; arrows limit the wavelength range covered by the "narrow" and "wide bands; c- Reference calibration curves for CIBR and N/W used for the sensitivity analysis.

Figure 2: Error introduced by least-square fitting to calibration laws: a- Comparison data/fit for CIBR; b- Comparison data/fit for N/W; c- Percent error between data and fit for CIBR and N/W.

Figure 3: Illustration of the interference of absorption features from typical ground reflectance (alfalfa, soil containing gypsum, and soil containing iron oxides) on atmospheric water bands.

Figure 4: Error introduced in amount of water retrieved by departure from gray background reflectance: a- Vegetation; b- Hydroxyl mineral such as gypsum; c- Iron oxides; d- Slight departure $(\mathrm{AR} = 0.01)$ from gray reflectance conditions for $0.01 \leq R \leq 0.05$; e- Slight departure from gray reflectance conditions for $0.05 \leq R \leq 0.70$; f- Gross departure from gray reflectance; g- Effect of liquid water absorption versus average gray reflectance.

Figure 5: Error introduced in amount of water retrieved for gross departure from reference meteorological range V = 25 km: a- 5 km: b- 50 km; c-1OO km; d- 250 km.

Figure 6: Slight changes in meteorological range ($\pm 1 \leq \Delta V \leq \pm 20$ km): a- for V_{ref} = 25 km; b- for V_{ref} = 50 km; c- for V_{ref} = 100 km; d- for V_{ref} = 250 km.

Figure 7: Error introduced in amount of water retrieved when using rural aerosols instead of: a- marine: b- urban.

Figure 8: Parameters used to describe viewing geometry for anisotropic aerosol scattering (see text for details).

Figure 9: Error due to anisotropic aerosol scattering and slant path attenuation: a- CIBR; b- NAN; c- Percent error in water amount retrieved.

Figure 10: Error introduced in amount of water retrieved due to: a- Shift in AVIRIS channel position in flight, CIBR; b- N/W; c- Change in AVIRIS band width in flight, CIBR; d- N/W.

Figure 11: a- Minimum recoverable fractional water abundances sW/W using the CIBR and N/W algorithms given an AVIRIS noise equivalent radiance of 0.06 mW/cm2/nm/sr as calculated from Equations (14) and (15); b- precipitable water differences as a function of W for the fractional abundances of (a).

Figure 12: Spatial concentration of vegetation at Salton Sea based on a Normalized Difference Vegetation Index (NDVI= $(L_{760} - L_{680})/(L_{760} + LIMO)$).

Figure 13: Location of the AVIRIS flight lines at Salton Sea. Circled cross shows location of Reagan sunphotometer measurements at the Salton Sea National Wildlife Refuge; rectangles locate AVIRIS images used for water recovery and shown on Figure 17.

Figure 14: a- Comparison of total column abundance of water retrieved in situ by the Reagan sunphotometer and AVIRIS data using the two techniques; b- Optical depths measured at Salton Sea; comparison Reagan/LOWTRAN 7. Open diamonds and squares represent limits of uncertainty from random plus coherent noise components present in the AVIRIS radiance data.

Figure 15: Comparison between NedL obtained from laboratory dark current measurements (average of 101 lines), inflight dark current measurements (average of 50 lines) and covariance matrix over a 50x50 pixel open water area.

Figure 16: Spatial distribution of total column abundance of water retrieved from AVIRIS data for the three overflights: a- CIBR; b- N/W; c- CIBR-N/W. A 5x5 median filter has been applied in order to decrease the noise effects.

Figure 17: a- Relationship between amount of green vegetation as estimated using the NDVI and amount of water retrieved by the two techniques. High NDVI represent green vegetation, negative NDVI, bare soils.

Figure 18: Reconciliation between observed and CIBR and N/W retrieved amounts of water after adjustment of model parameters for the SSNWR site.

Figure 19: Comparison between LOWTRAN 7 adjusted and AVIRIS observed radiances for the SSNWR site for the first AVIRIS overpass. Parameters used to constrain LOWTRAN 7 are: Flight dir. = N140; Across track az. = N315; 14° off-nadir; H20 = 2.795 cm; R = 0.21: v = 190 km; rural aerosols.

FIGURE 1

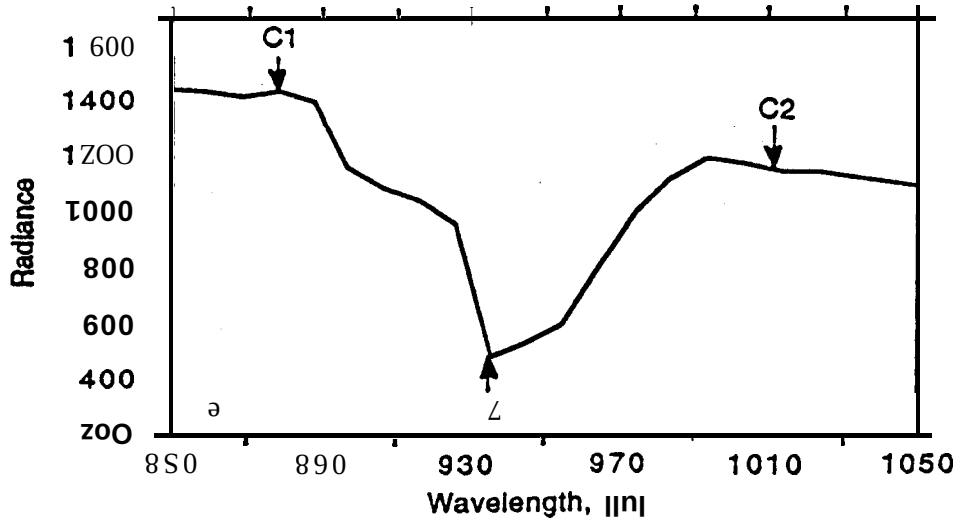
C1
C2
Radiance
1400
1200
1000
800
600
400
850
890
930
970
1010
1050
Wavelength, nm

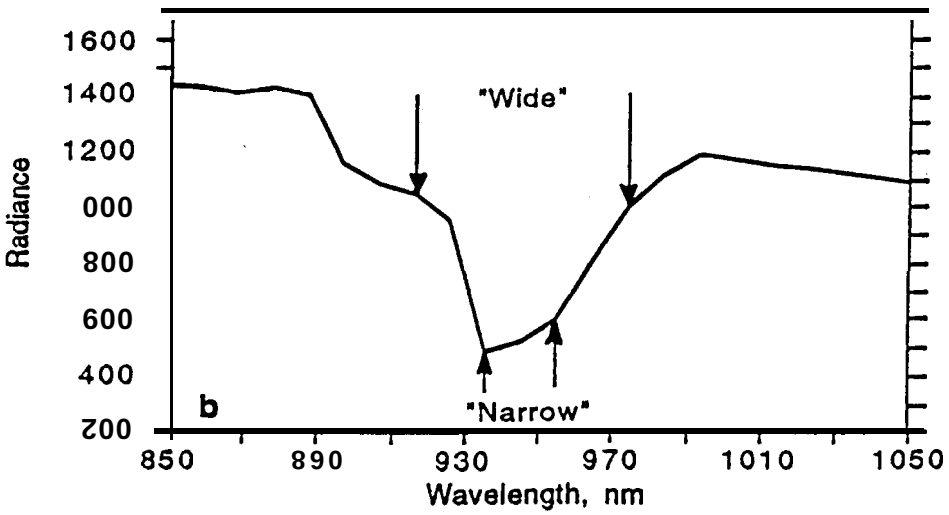
"Wide"
"Narrow"
b
Radiance
1600
1400
1200
800
600
400
850
890
930
970
1010
1050
Wavelength, nm

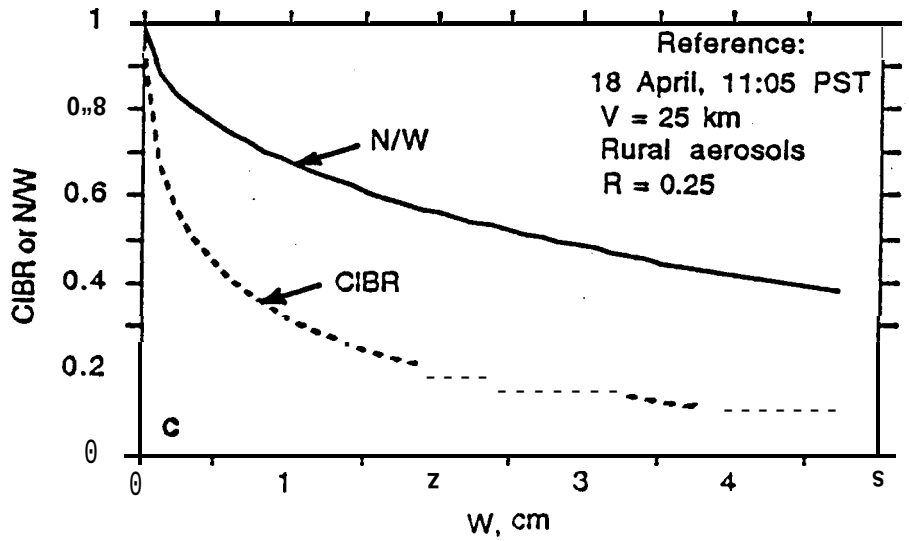
Reference:
18 April, 11:05 PST
V = 25 km
Rural aerosols
R = 0.25
N/W
CIBR
c
CIBR or N/W
1
0.8
0.6
0.4
0.2
0
1
2
3
4
W, cm

FIGURE 2

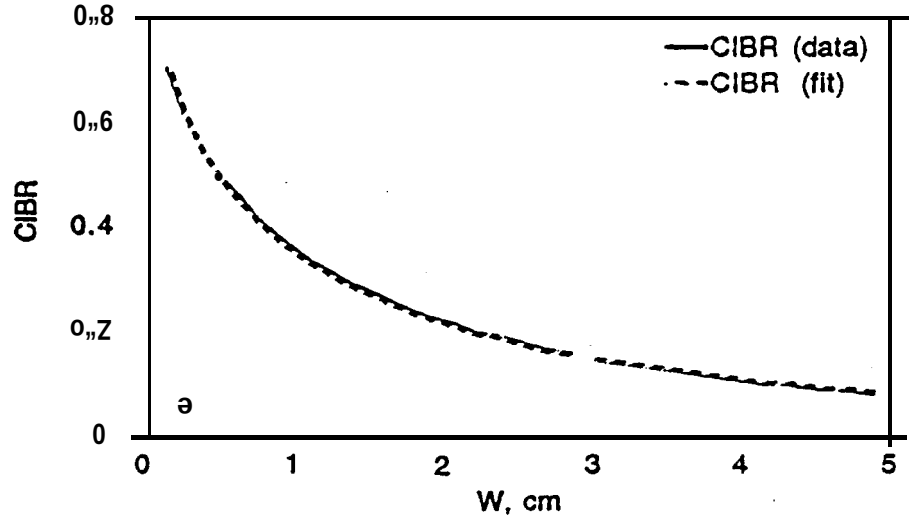
0„8
0„6
0.4
0„Z
0
CIBR
—CIBR (data)
- -CIBR (fit)
ə
0
1
2
3
4
5
W, cm

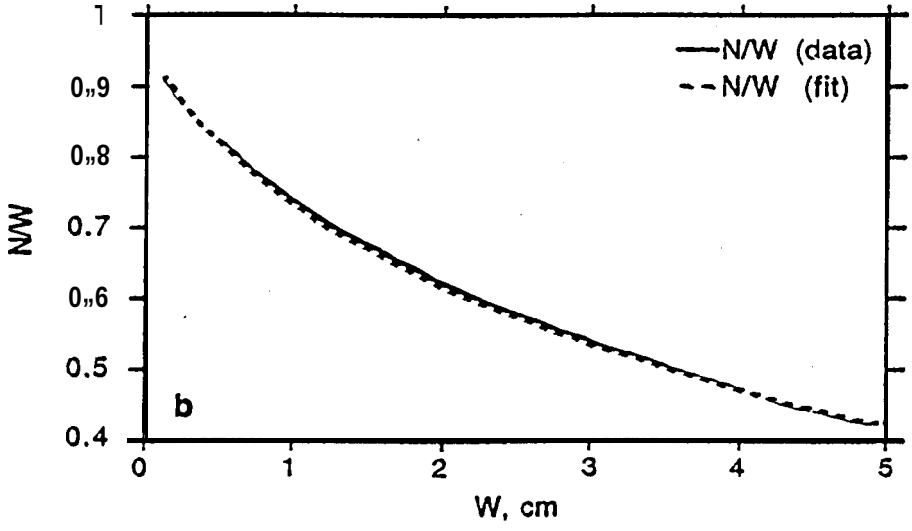
1
0„9
0„8
0.7
0„6
0.5
0.4
N/W
—N/W (data)
- -N/W (fit)
b
0
1
2
3
4
5
W, cm

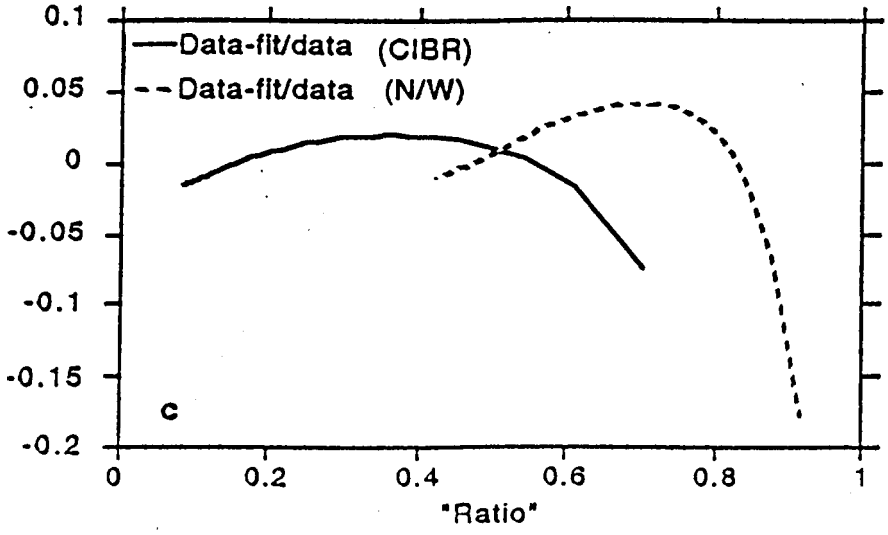
0.1
0.05
0
-0.05
-0.1
-0.15
-0.2
—Data-fit/data (CIBR)
- -Data-fit/data (N/W)
c
0
0.2
0.4
0.6
0.8
1
"Ratio"

FIGURE 3

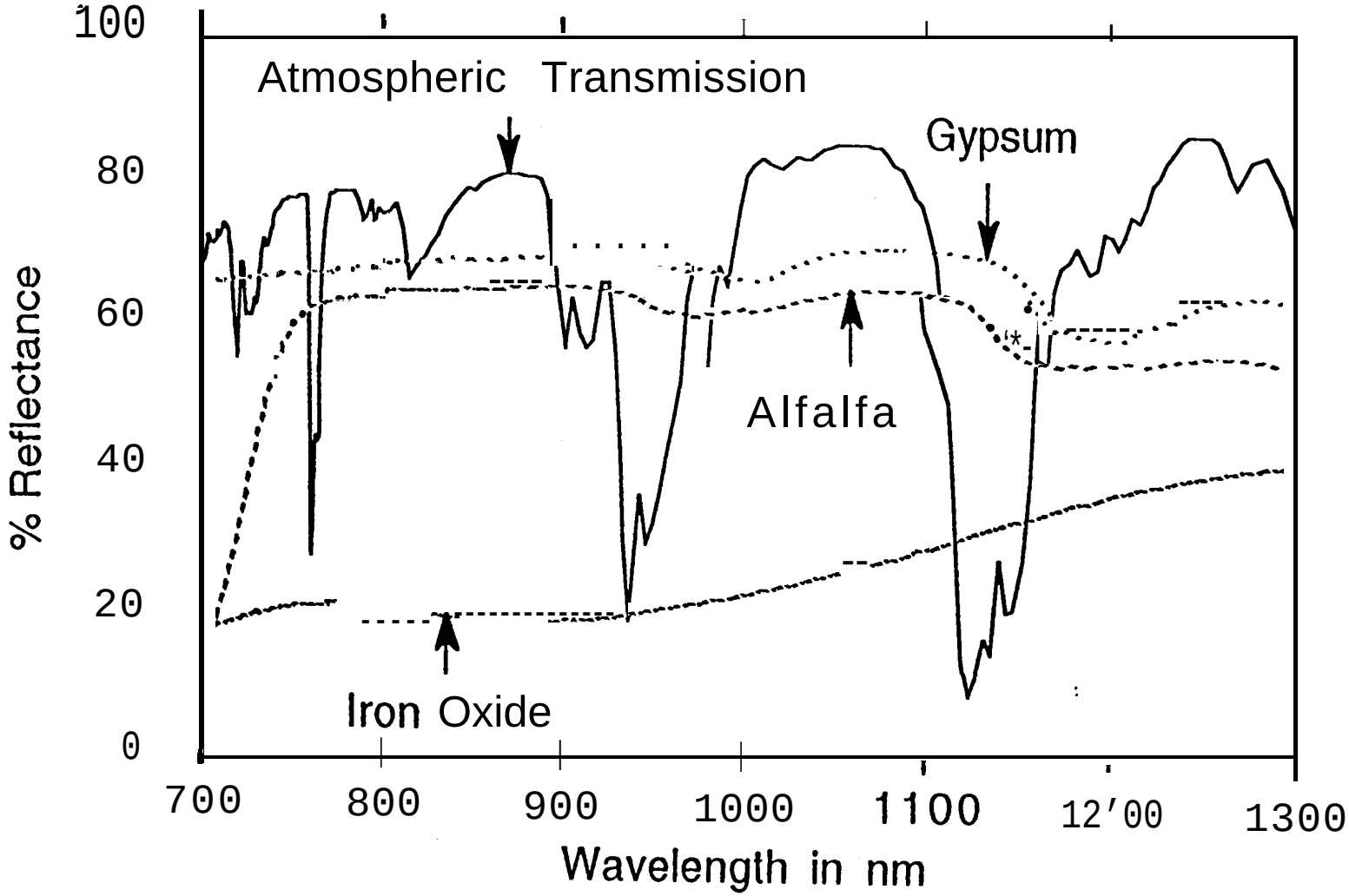
100
80
60
40
20
0
% Reflectance
Atmospheric Transmission
Gypsum
Alfalfa
Iron Oxide
700
800
900
1000
1100
12'00
1300
Wavelength in nm

FIGURE 4 (I)

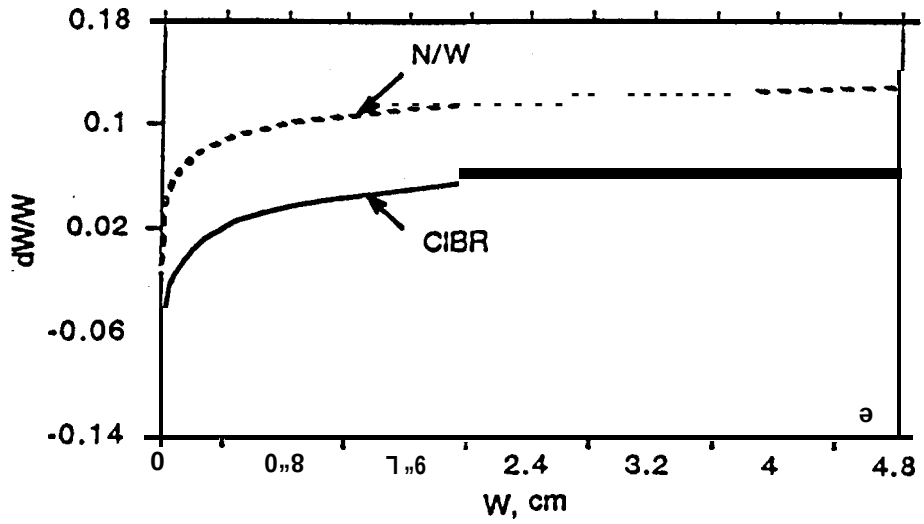
0.18
0.1
0.02
-0.06
-0.14
dW/W
N/W
CIBR
0
0.8
1.6
2.4
3.2
4
4.8
W, cm
a

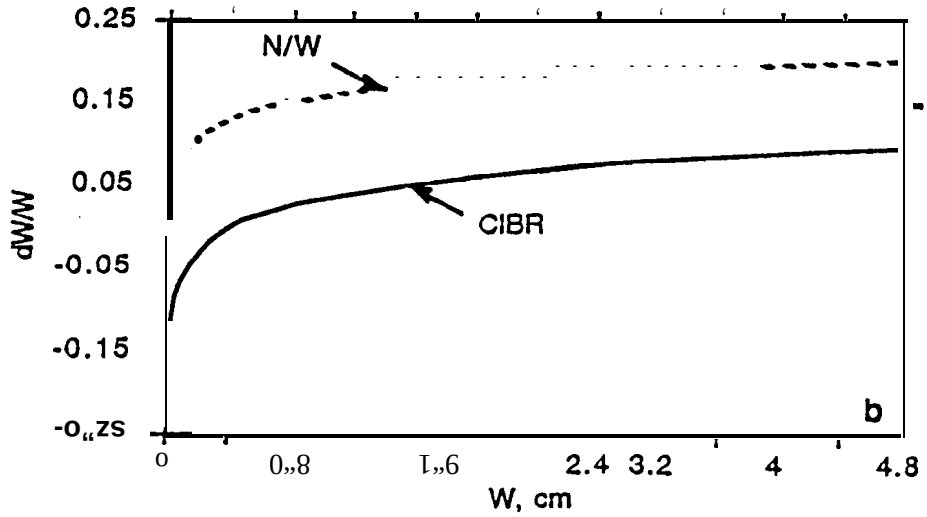
0.25
0.15
0.05
-0.05
-0.15
dW/W
N/W
CIBR
0
0.8
1.6
2.4
3.2
4
4.8
W, cm
b

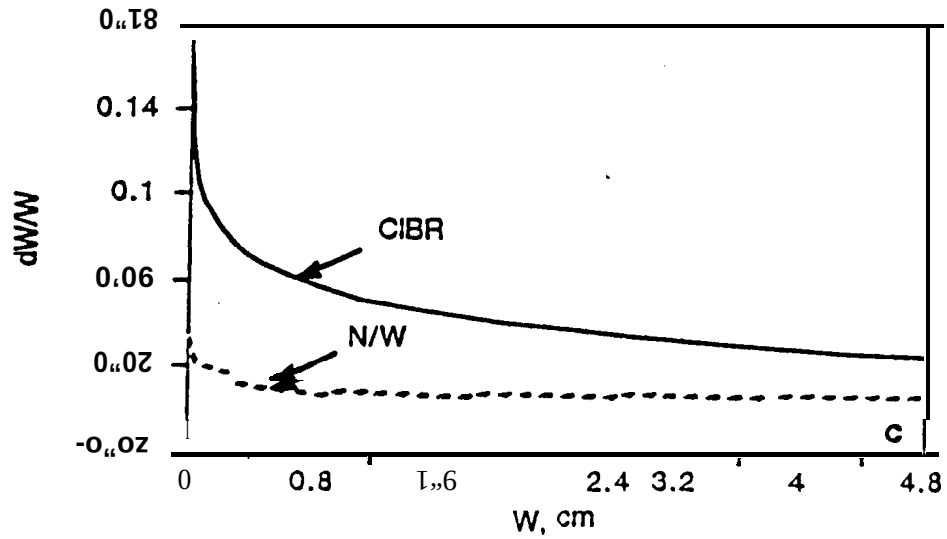
0.18
0.14
0.1
0.06
0.02
-0.02
dW/W
CIBR
N/W
0
0.8
1.6
2.4
3.2
4
4.8
W, cm
c

FIGURE 4 (II)

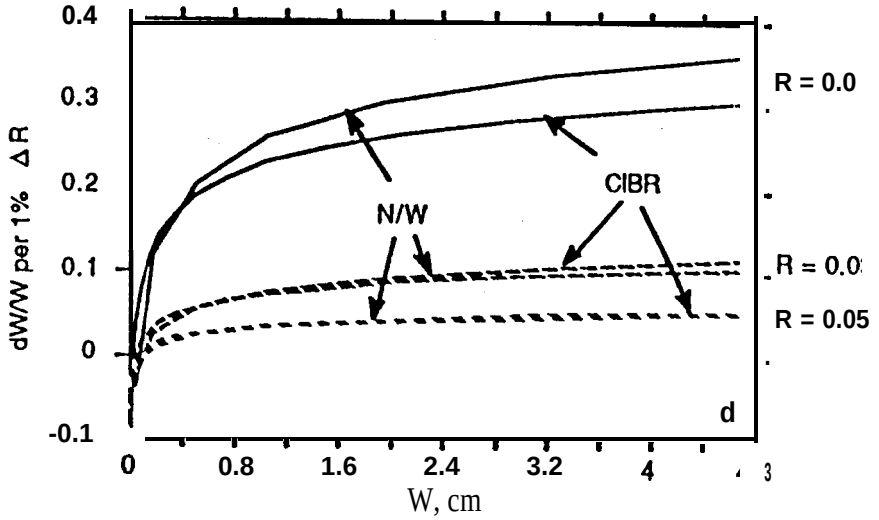
dW/W per 1% ΔR
0.4
0.3
0.2
0.1
0
-0.1
N/W
CIBR
R = 0.0
R = 0.0
R = 0.05
d
0
0.8
1.6
2.4
3.2
4
W, cm

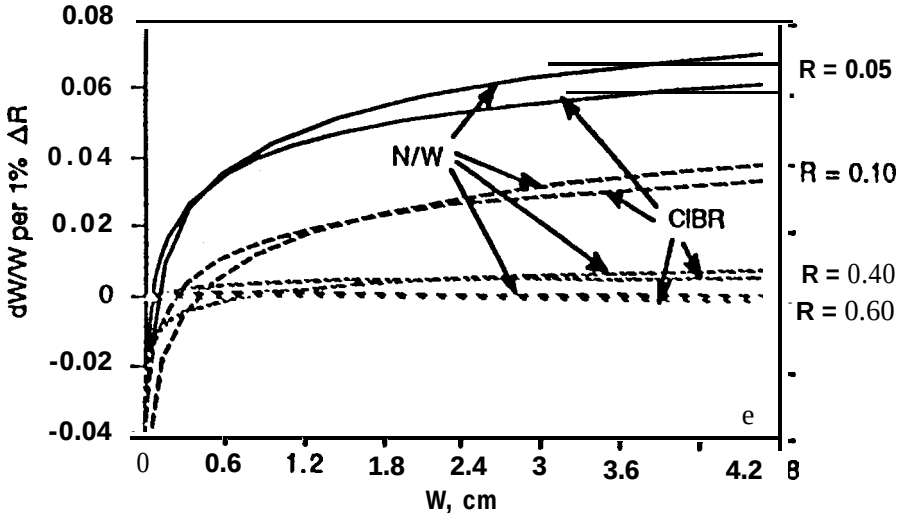
dW/W per 1% ΔR
0.08
0.06
0.04
0.02
0
-0.02
-0.04
N/W
CIBR
R = 0.05
R = 0.10
R = 0.40
R = 0.60
e
0
0.6
1.2
1.8
2.4
3
3.6
4.2
W, cm

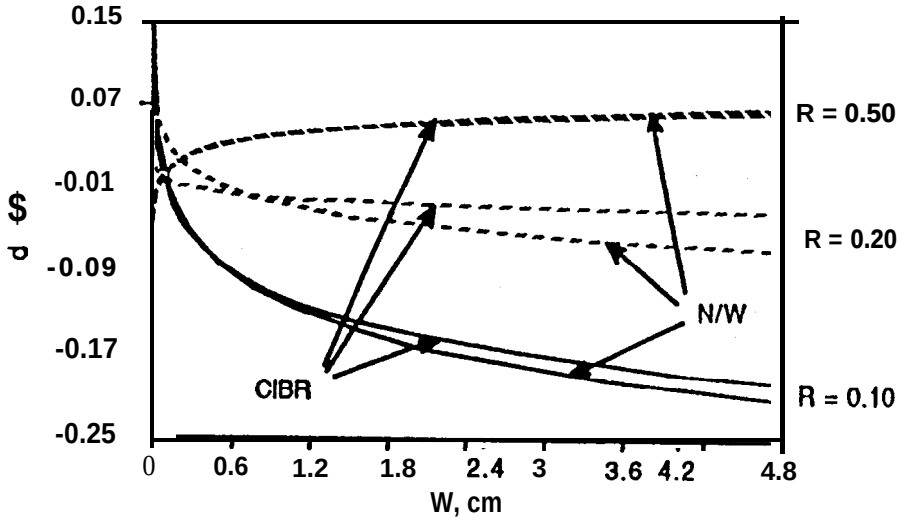
d $
0.15
0.07
-0.01
-0.09
-0.17
-0.25
CIBR
N/W
R = 0.50
R = 0.20
R = 0.10
0
0.6
1.2
1.8
2.4
3
3.6
4.2
4.8
W, cm

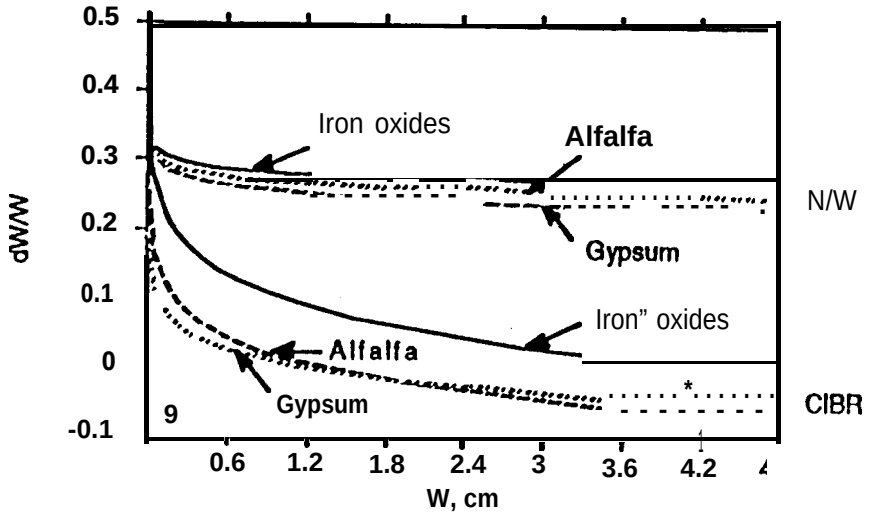
dW/W
0.5
0.4
0.3
0.2
0.1
0
-0.1
Iron oxides
Alfalfa
Gypsum
N/W
Iron" oxides
Alfalfa
Gypsum
CIBR
9
0.6
1.2
1.8
2.4
3
3.6
4.2
W, cm

FIGURE 5

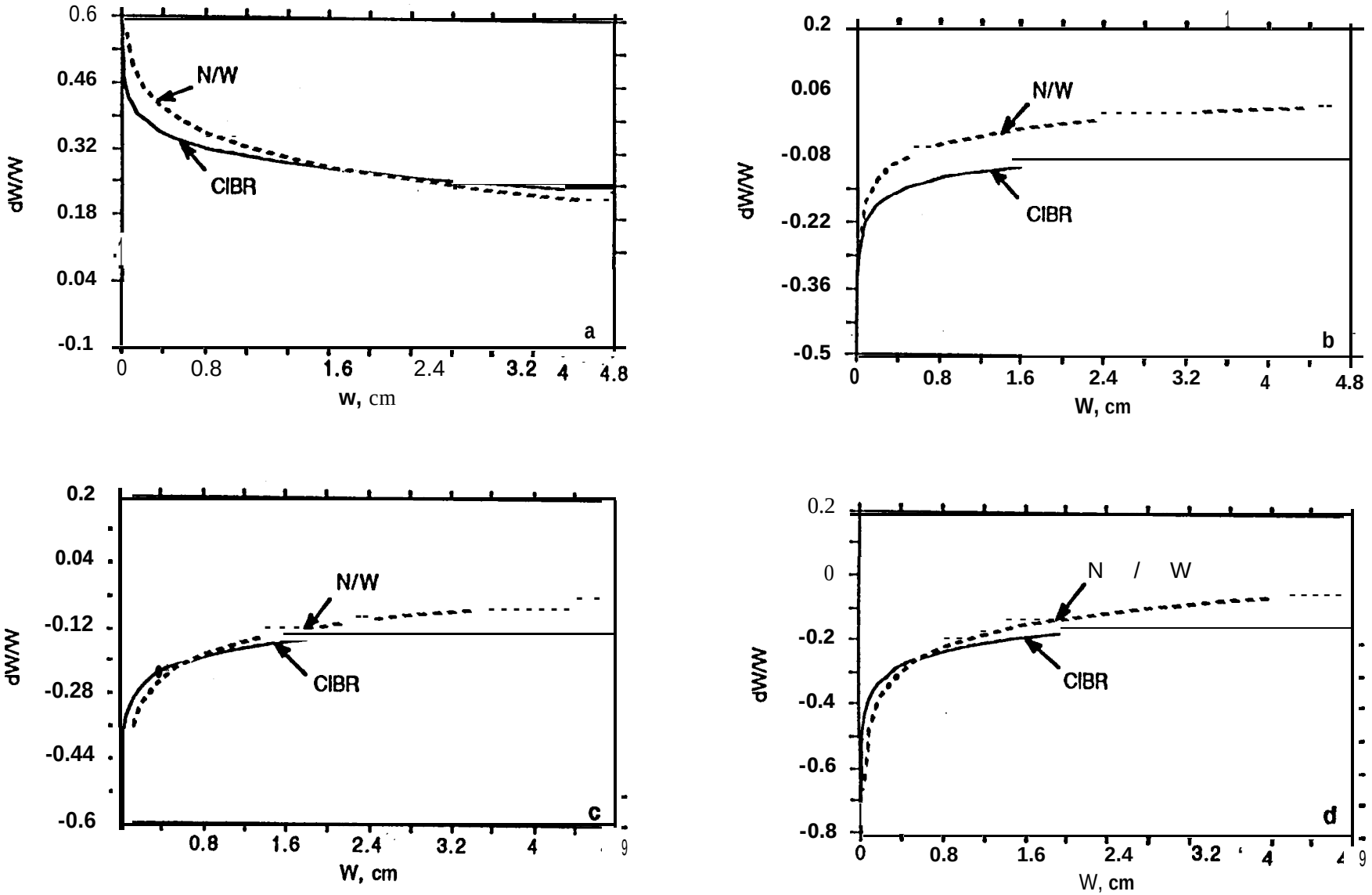
0.6
0.46
0.32
0.18
0.04
-0.1
dW/W
N/W
CIBR
a
0
0.8
1.6
2.4
3.2
4
4.8
w, cm
0.2
0.06
-0.08
-0.22
-0.36
-0.5
dW/W
N/W
CIBR
b
0
0.8
1.6
2.4
3.2
4
4.8
W, cm
0.2
0.04
-0.12
-0.28
-0.44
-0.6
dW/W
N/W
CIBR
c
0.8
1.6
2.4
3.2
4
W, cm
0.2
0
-0.2
-0.4
-0.6
-0.8
dW/W
N / W
CIBR
d
0
0.8
1.6
2.4
3.2
4
W, cm

FIGURE 6

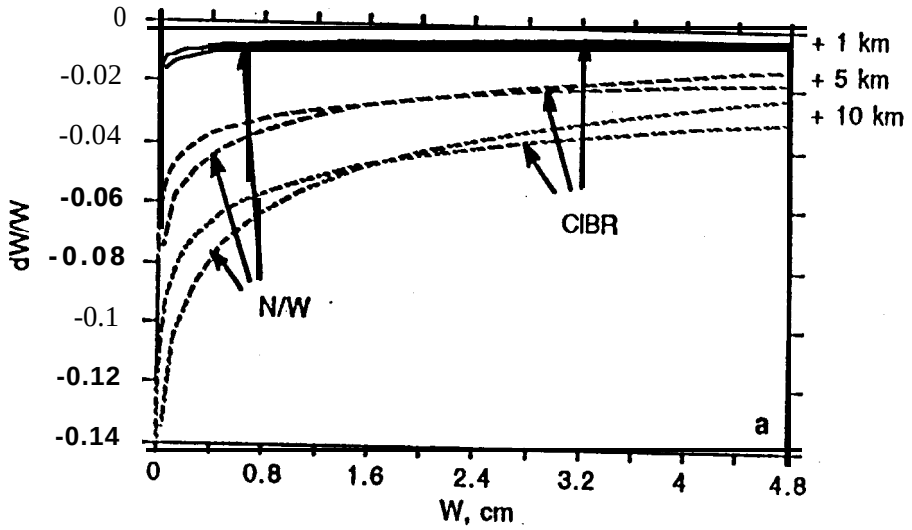
0
-0.02
-0.04
-0.06
-0.08
-0.1
-0.12
-0.14
dW/W
+ 1 km
+ 5 km
+ 10 km
CIBR
N/W
a
0
0.8
1.6
2.4
3.2
4
4.8
W, cm

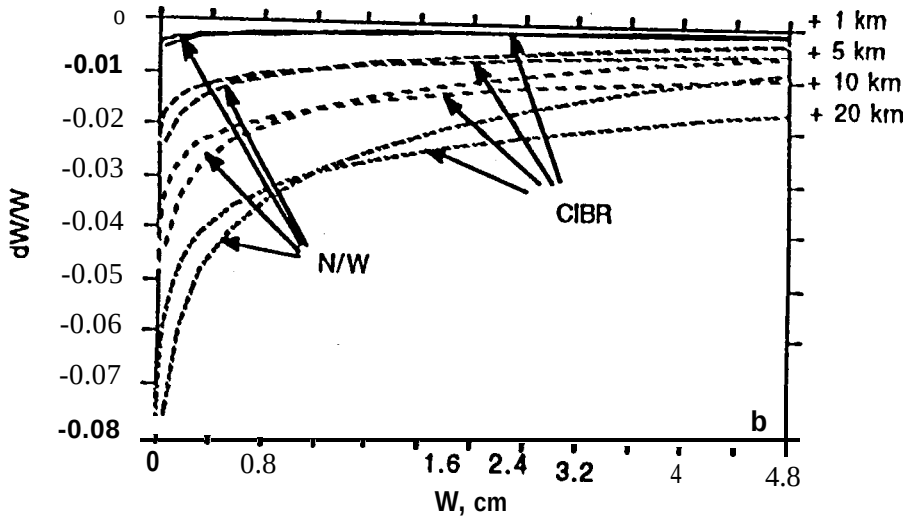
0
-0.01
-0.02
-0.03
-0.04
-0.05
-0.06
-0.07
-0.08
dW/W
+ 1 km
+ 5 km
+ 10 km
+ 20 km
CIBR
N/W
b
0
0.8
1.6
2.4
3.2
4
4.8
W, cm

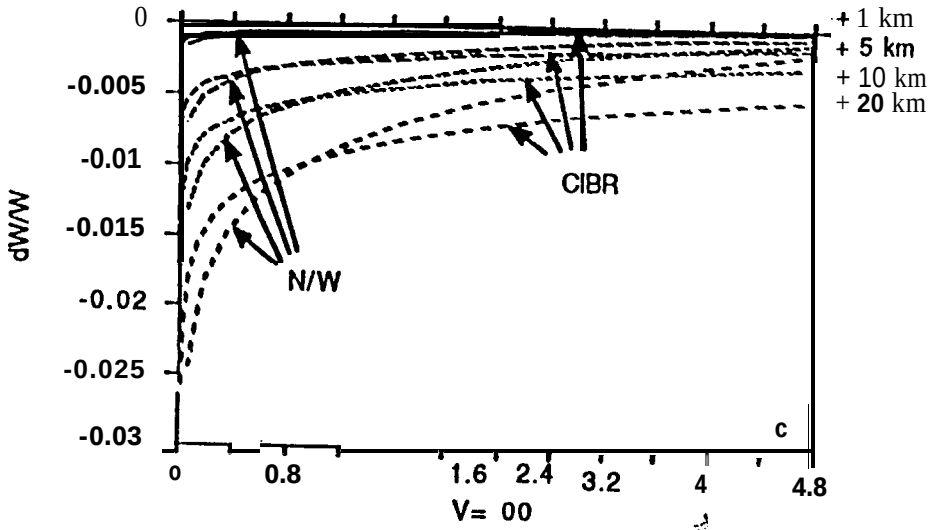
0
-0.005
-0.01
-0.015
-0.02
-0.025
-0.03
dW/W
+ 1 km
+ 5 km
+ 10 km
+ 20 km
CIBR
N/W
c
0
0.8
1.6
2.4
3.2
4
4.8
V= 00

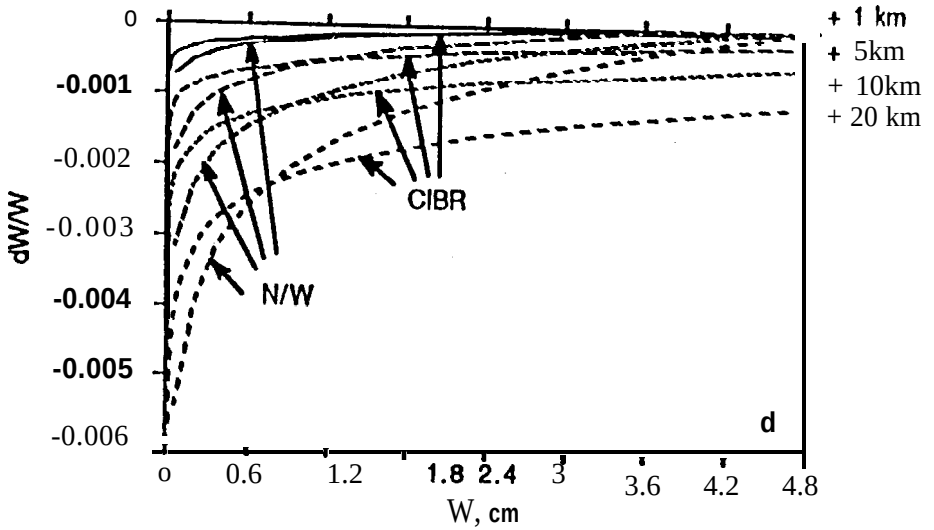
0
-0.001
-0.002
-0.003
-0.004
-0.005
-0.006
dW/W
+ 1 km
+ 5km
+ 10km
+ 20 km
CIBR
N/W
d
0
0.6
1.2
1.8
2.4
3
3.6
4.2
4.8
W, cm

FIGURE 7

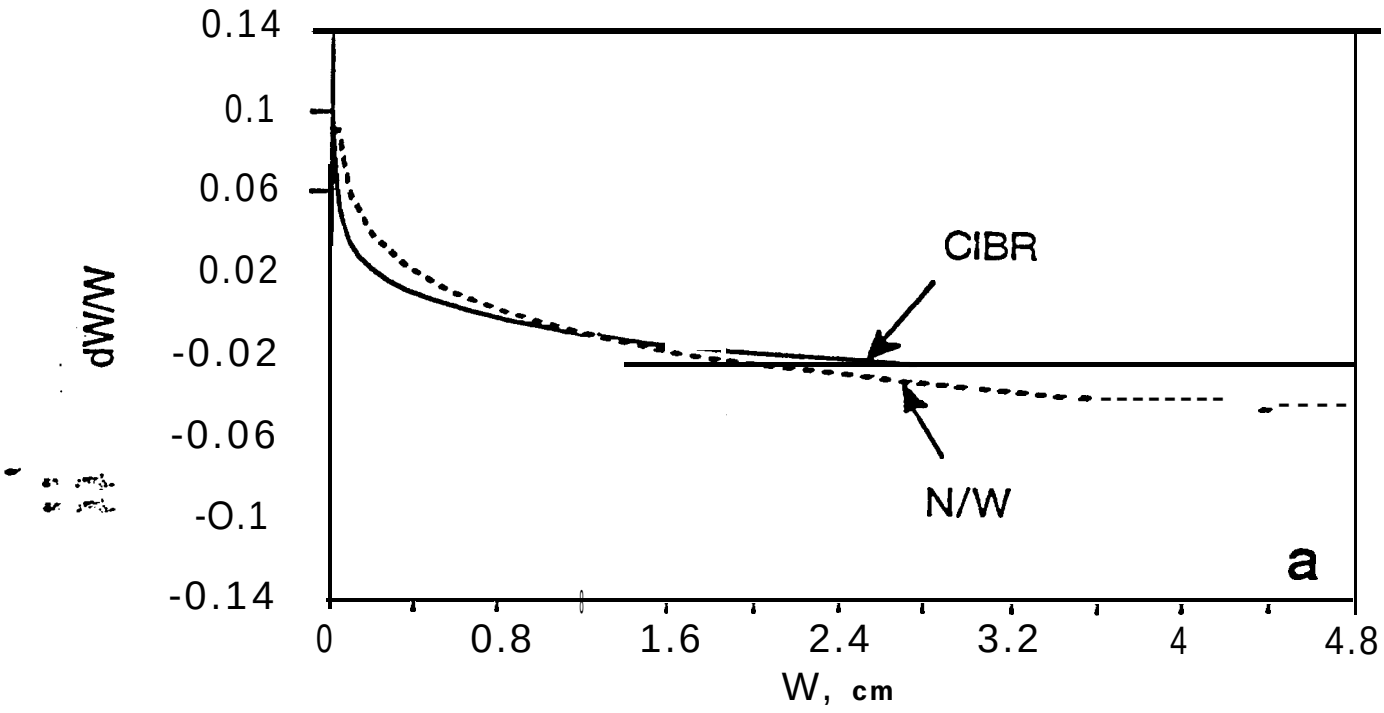
0.14
0.1
0.06
0.02
-0.02
-0.06
-O.1
-0.14
dW/W
CIBR
N/W
a
0
0.8
1.6
2.4
3.2
4
4.8
W, cm

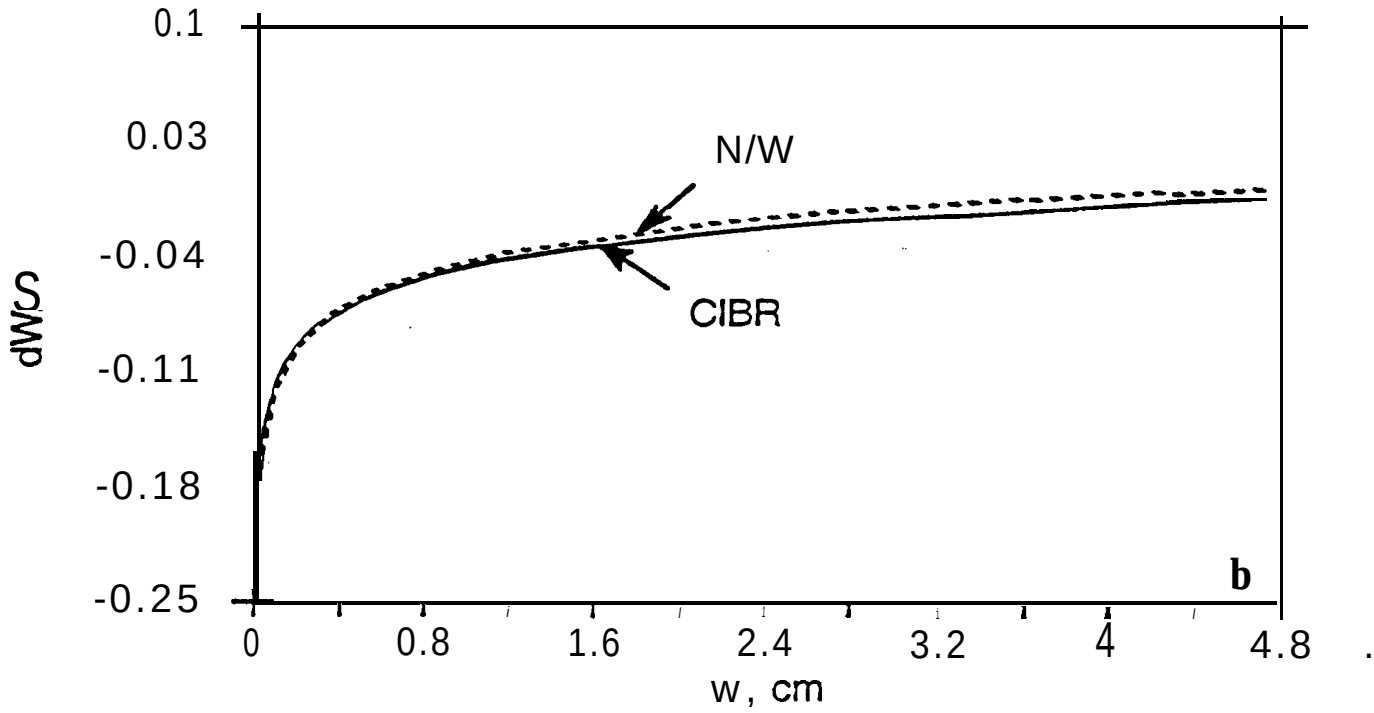
0.1
0.03
-0.04
-0.11
-0.18
-0.25
dWS
N/W
CIBR
b
0
0.8
1.6
2.4
3.2
4
4.8
w, cm

FIGURE 8

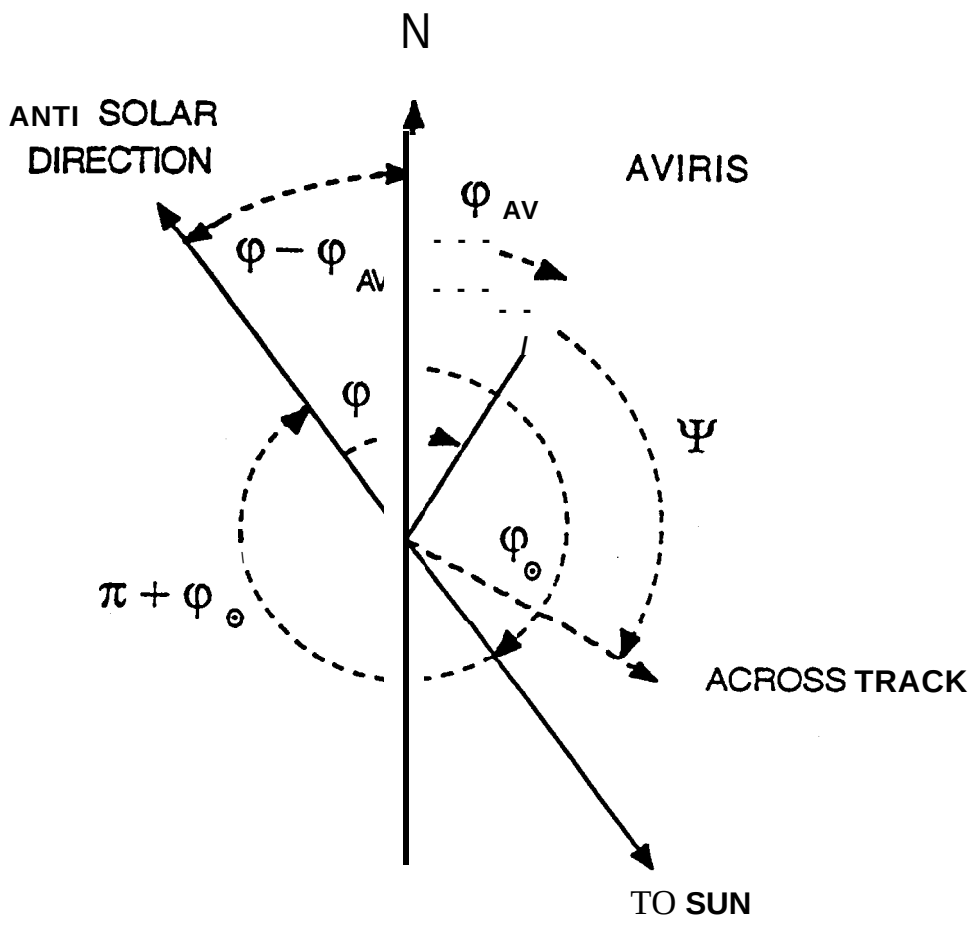
N
ANTI SOLAR DIRECTION
AVIRIS
φ_{AV}
$\varphi - \varphi_{AV}$
φ
Ψ
$\varphi_{\odot}$
$\pi + \varphi_{\odot}$
ACROSS TRACK
TO SUN

FIGURE 9

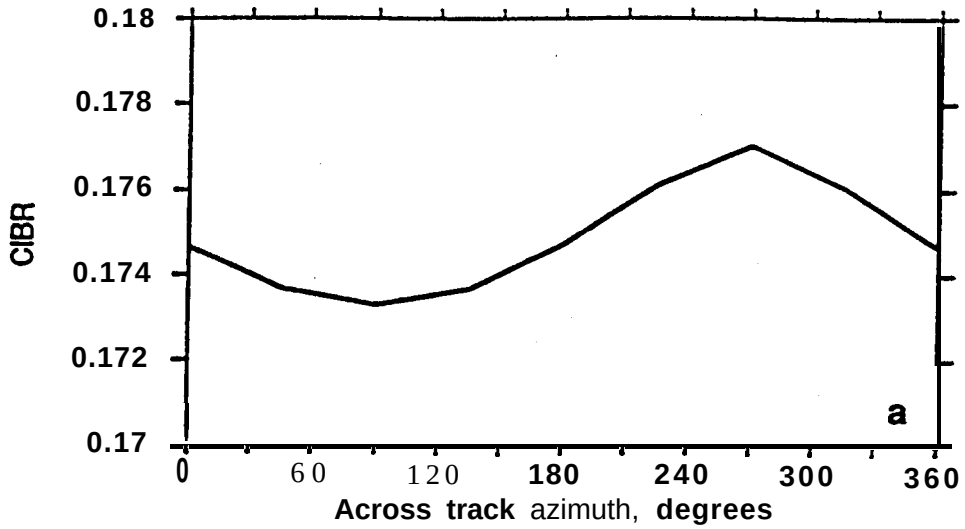
0.18
0.178
0.176
0.174
0.172
0.17
CIBR
a
0
60
120
180
240
300
360
Across track azimuth, degrees

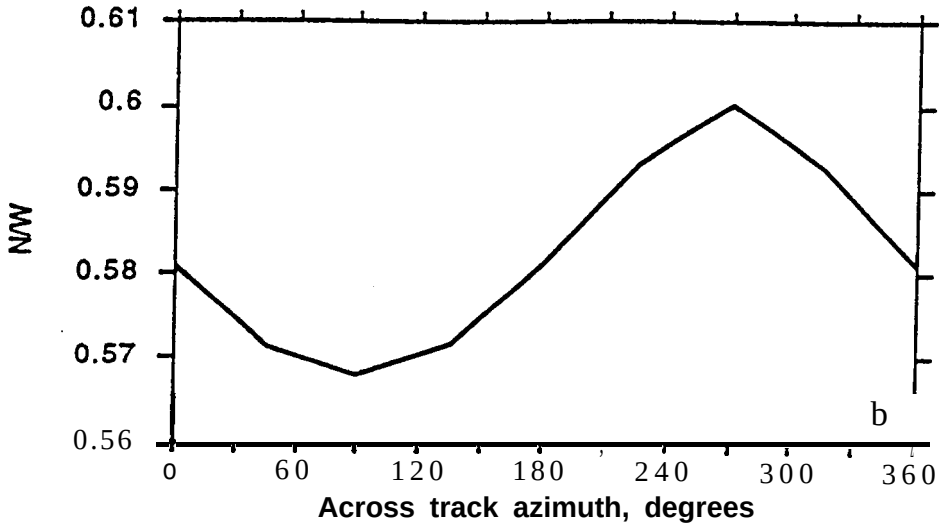
0.61
0.6
0.59
0.58
0.57
0.56
N/W
b
0
60
120
180
240
300
360
Across track azimuth, degrees

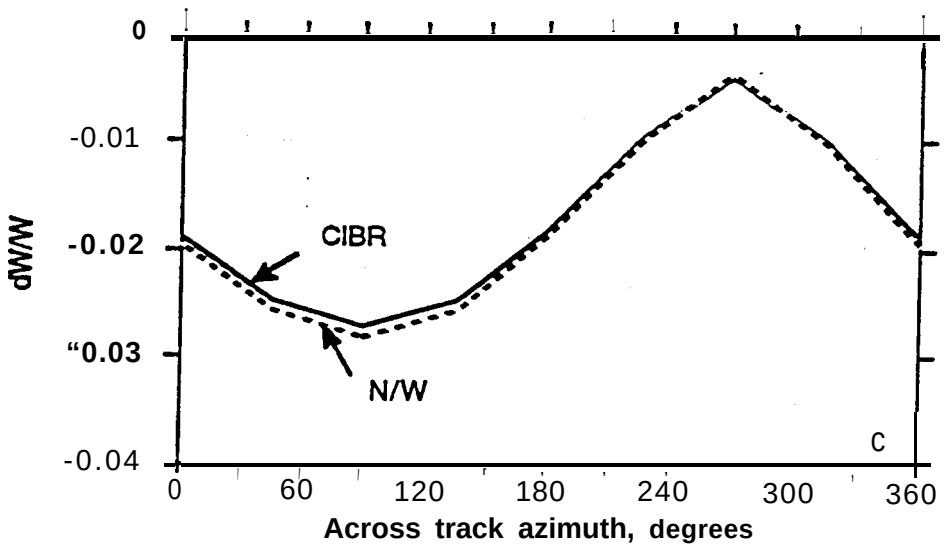
0
-0.01
-0.02
"0.03
-0.04
dW/W
CIBR
N/W
c
0
60
120
180
240
300
360
Across track azimuth, degrees

FIGURE 10

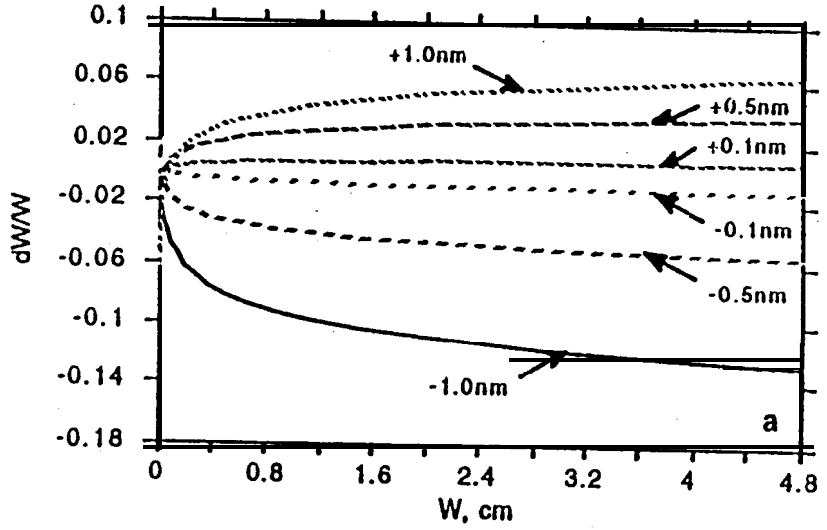
0.1
0.06
0.02
-0.02
-0.06
-0.1
-0.14
-0.18
dW/W
+1.0nm
+0.5nm
+0.1nm
-0.1nm
-0.5nm
-1.0nm
a
0
0.8
1.6
2.4
3.2
4
4.8
W, cm

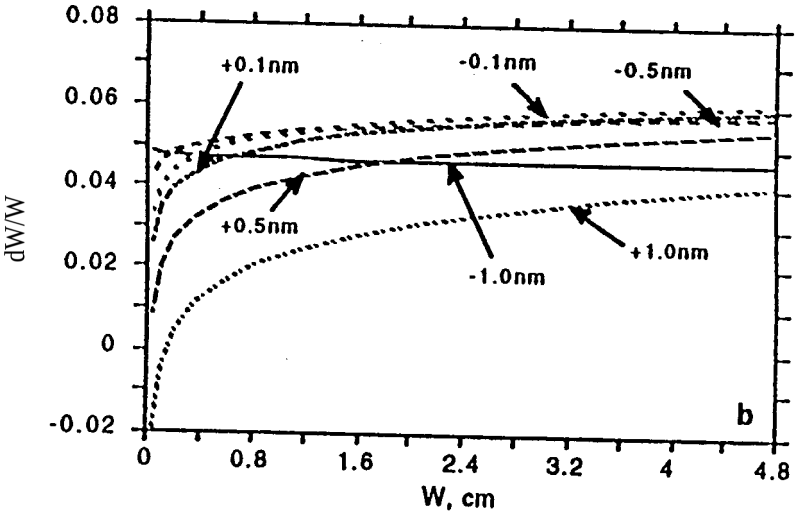
0.08
0.06
0.04
0.02
0
-0.02
dW/W
+0.1nm
-0.1nm
-0.5nm
+0.5nm
-1.0nm
+1.0nm
b
0
0.8
1.6
2.4
3.2
4
4.8
W, cm

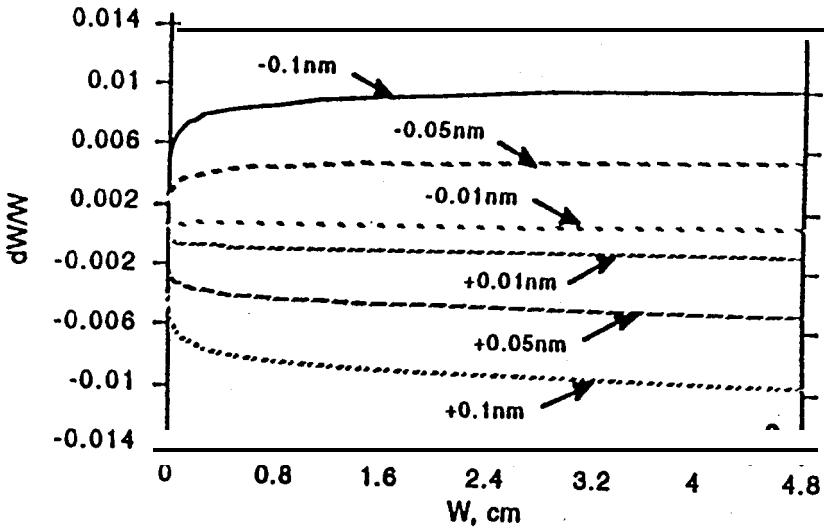
0.014
0.01
0.006
0.002
-0.002
-0.006
-0.01
-0.014
dW/W
-0.1nm
-0.05nm
-0.01nm
+0.01nm
+0.05nm
+0.1nm
0
0.8
1.6
2.4
3.2
4
4.8
W, cm

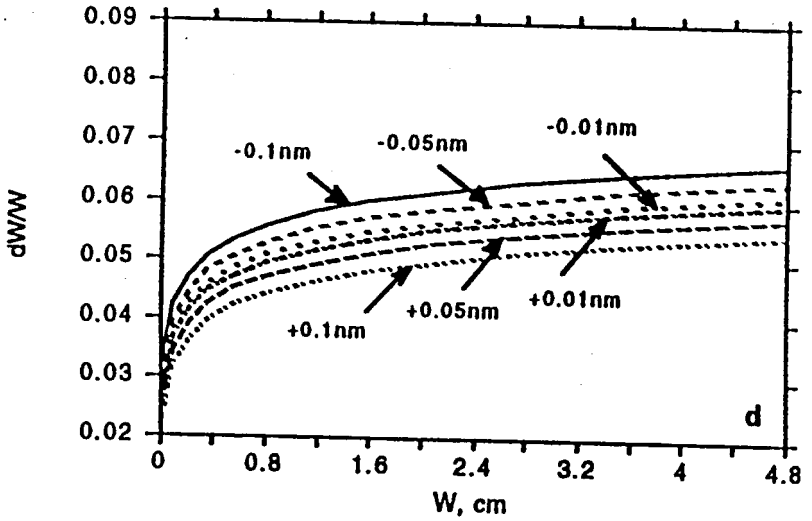
0.09
0.08
0.07
0.06
0.05
0.04
0.03
0.02
dW/W
-0.1nm
-0.05nm
-0.01nm
+0.1nm
+0.05nm
+0.01nm
d
0
0.8
1.6
2.4
3.2
4
4.8
W, cm

FIG 11

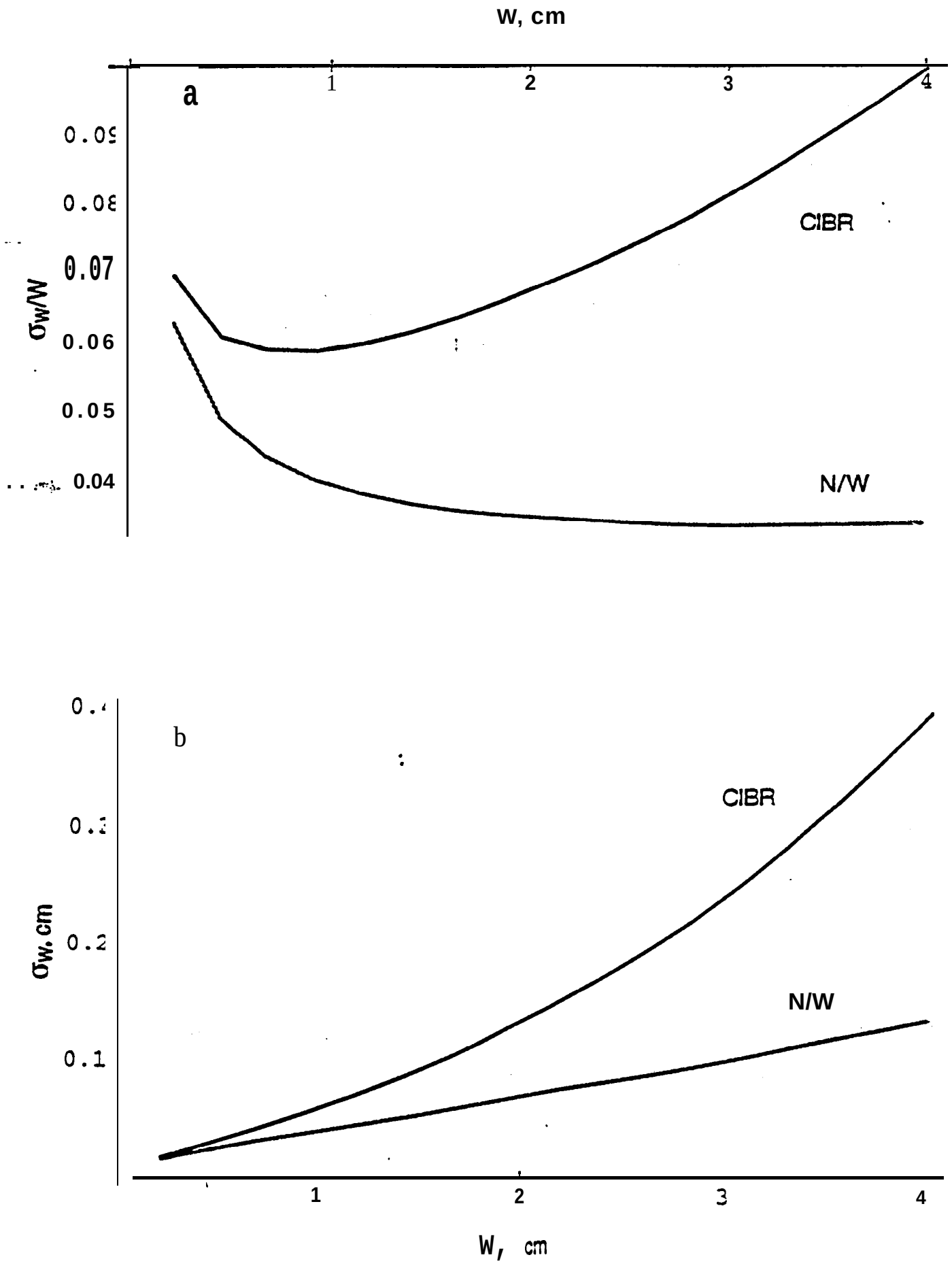
W, cm
a
1
2
3
4
0.09
0.08
0.07
0.06
0.05
0.04
σW/W
CIBR
N/W
b
0.4
0.3
0.2
0.1
σW, cm
CIBR
N/W
1
2
3
4
W, cm

FIGURE 2

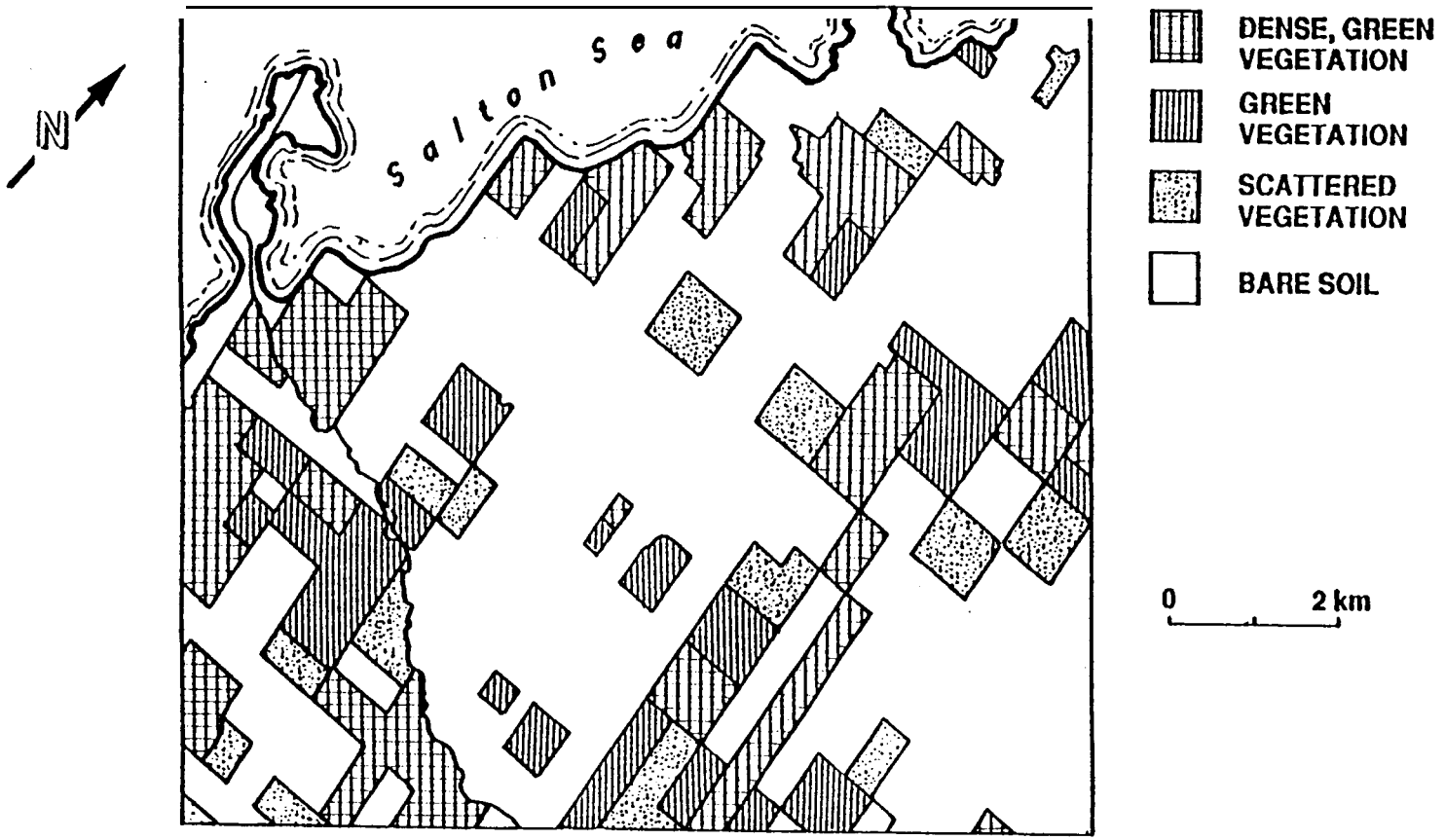
N
Salton Sea
DENSE, GREEN VEGETATION
GREEN VEGETATION
SCATTERED VEGETATION
BARE SOIL
0
2 km

FIGURE 13

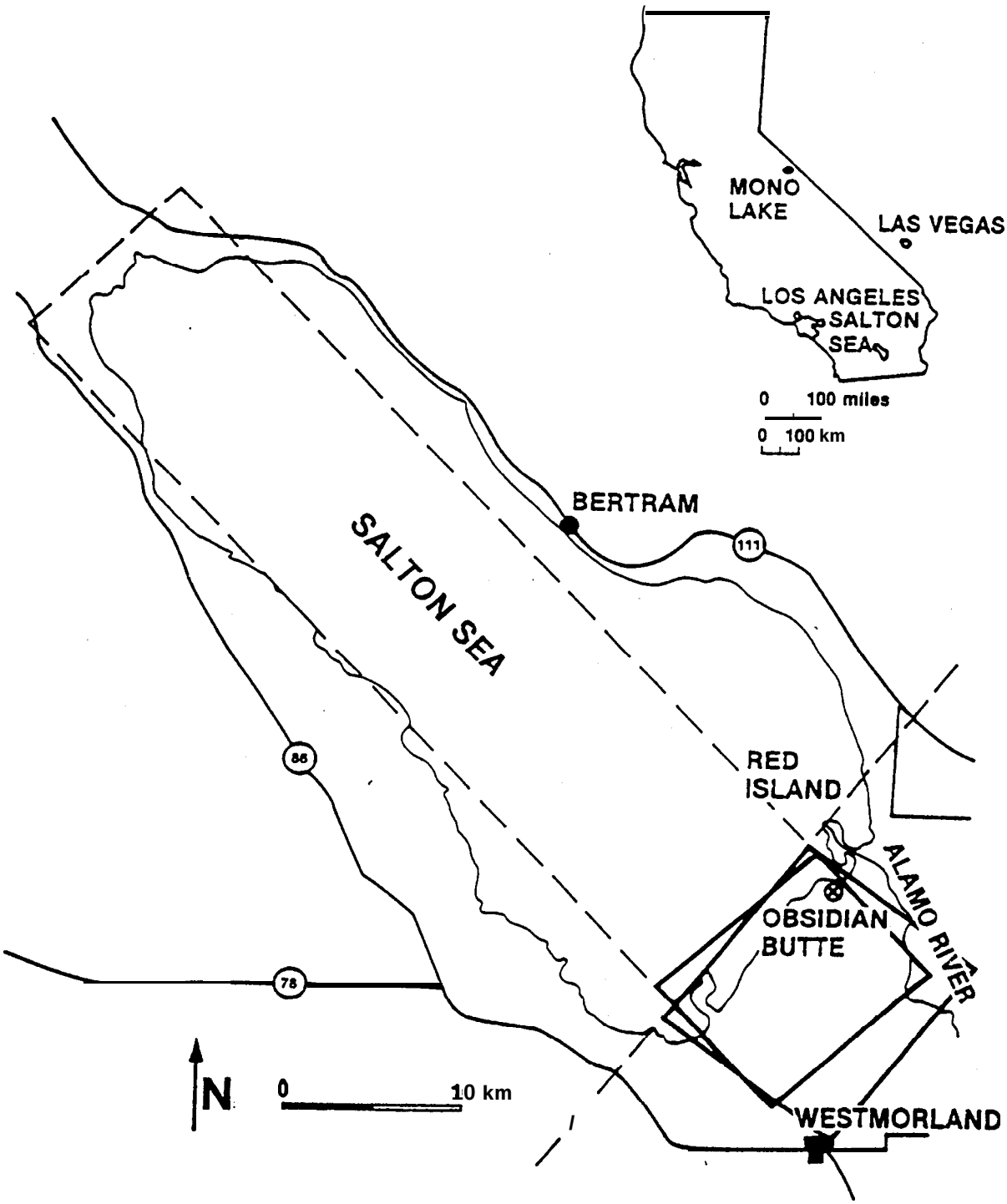
MONO LAKE
LAS VEGAS
LOS ANGELES
SALTON SEA
0 100 miles
0 100 km
BERTRAM
SALTON SEA
111
86
RED ISLAND
ALAMO RIVER
OBSIDIAN BUTTE
78
N
0 10 km
WESTMORLAND

FIGURE 14

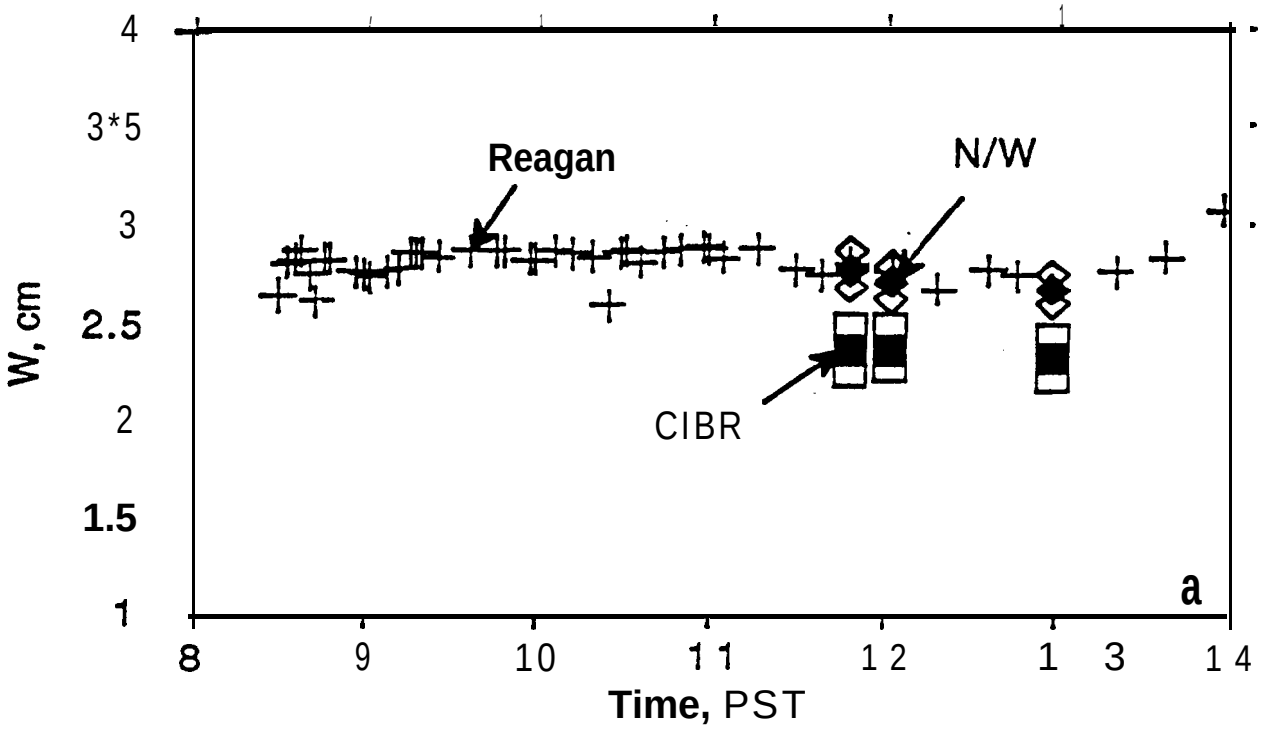
4
3*5
3
2.5
2
1.5
1
W, cm
Reagan
N/W
CIBR
a
8
9
10
11
12
1
3
14
Time, PST

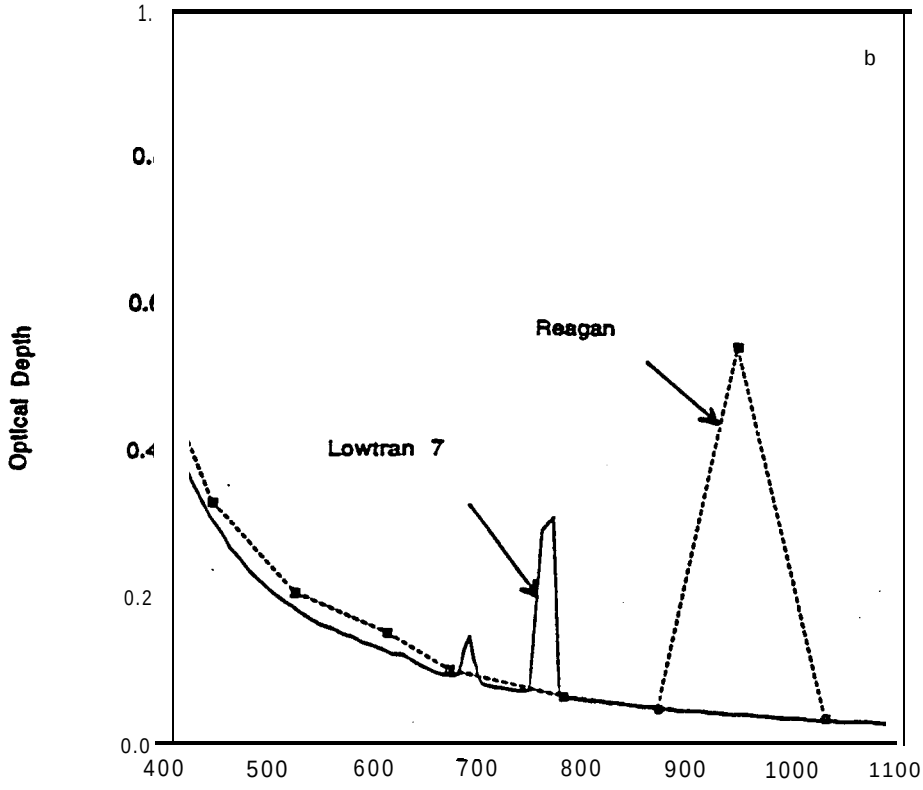
1.
0.
0.
0.4
0.2
0.0
Optical Depth
b
Reagan
Lowtran 7
400
500
600
700
800
900
1000
1100
Wavelength in nm

FIGURE 15

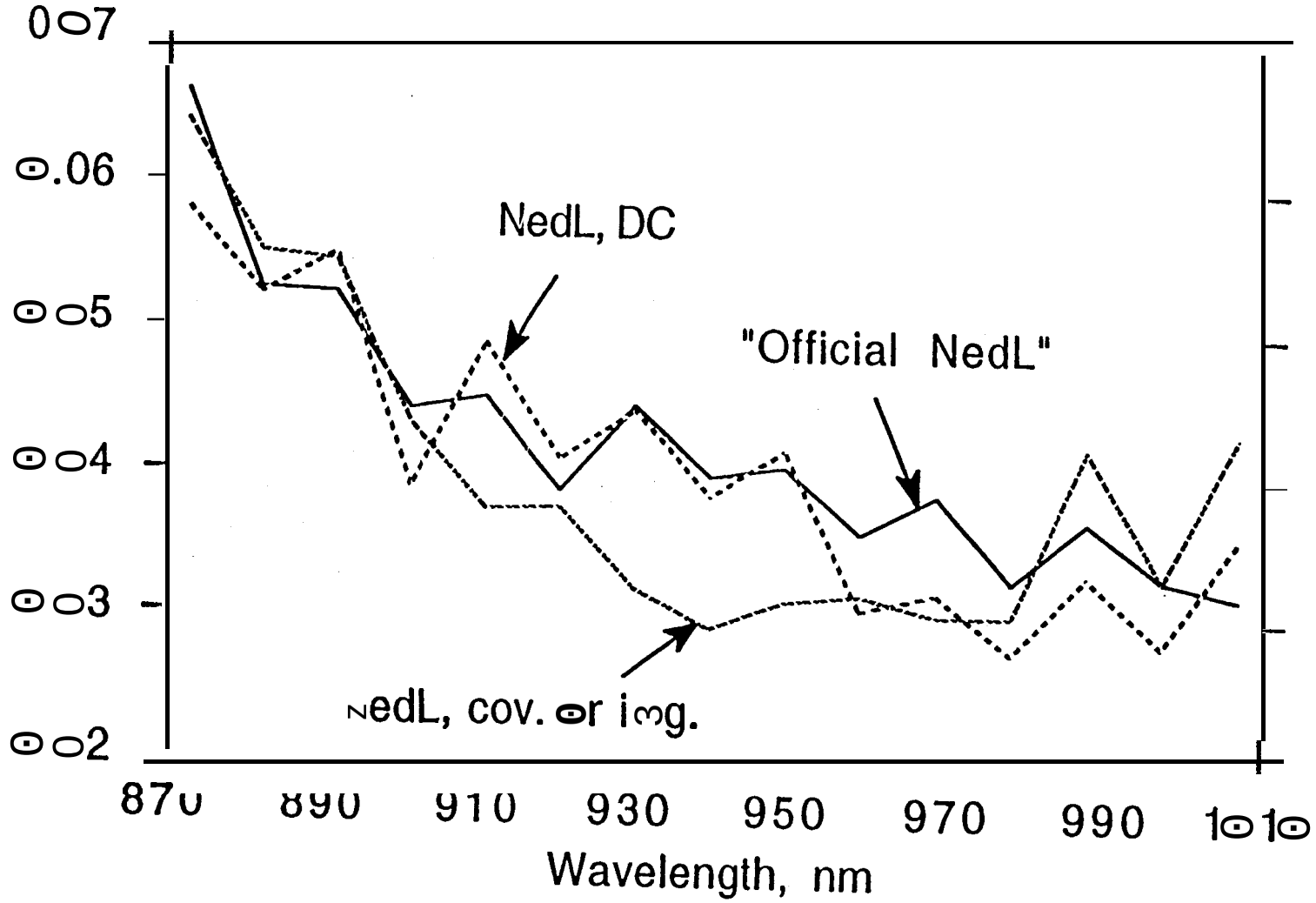
007
⊙.06
⊙05
⊙04
⊙03
⊙02
NedL, DC
"Official NedL"
NedL, cov. or img.
870
890
910
930
950
970
990
1010
Wavelength, nm

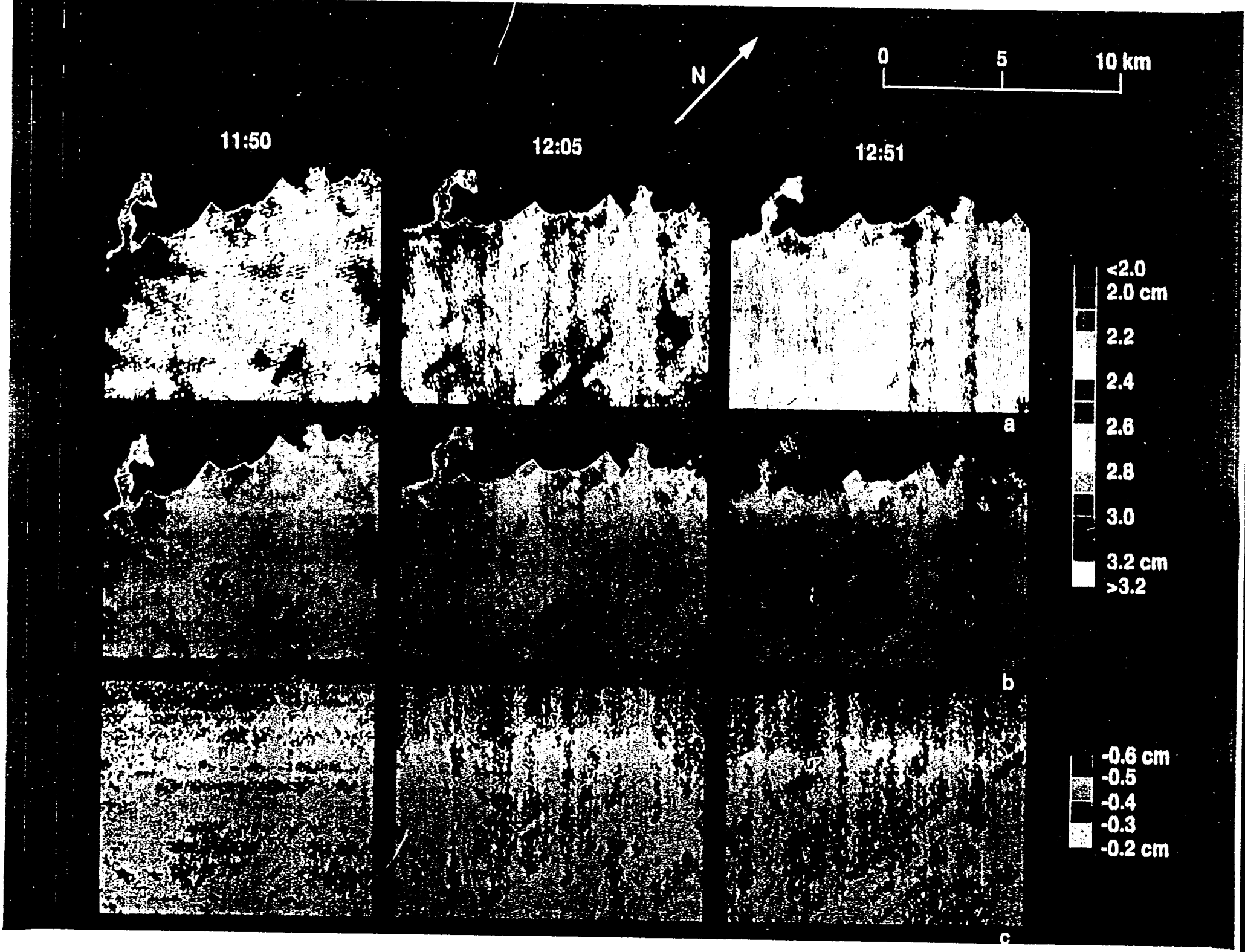
N
0
5
10 km
11:50
12:05
12:51
a
b
c
<2.0
2.0 cm
2.2
2.4
2.6
2.8
3.0
3.2 cm
>3.2
-0.6 cm
-0.5
-0.4
-0.3
-0.2 cm

FIGURE 17

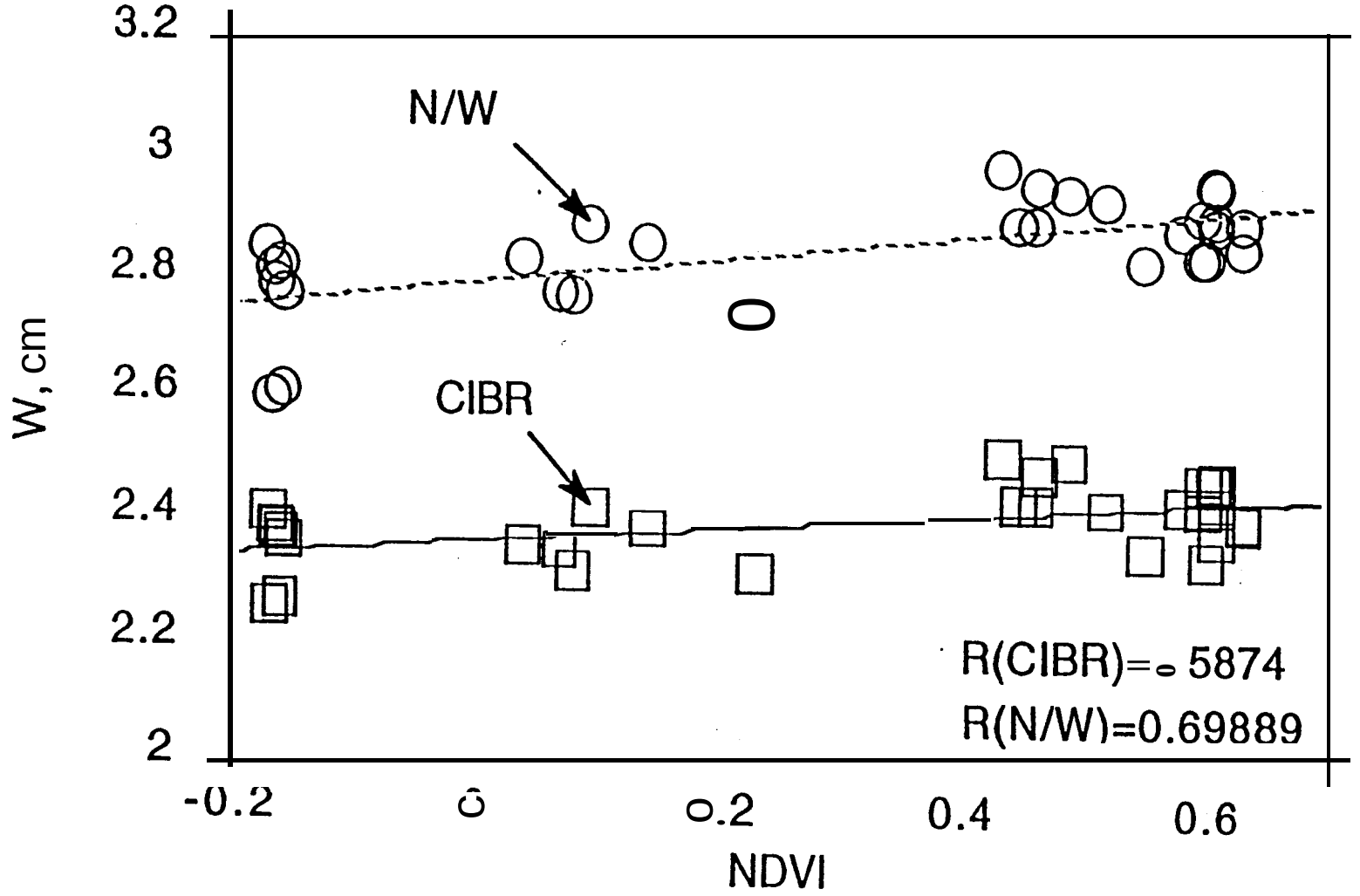
3.2
3
2.8
2.6
2.4
2.2
2
W, cm
N/W
CIBR
R(CIBR)=0.5874
R(N/W)=0.69889
-0.2
0
0.2
0.4
0.6
NDVI

FIGURE 9

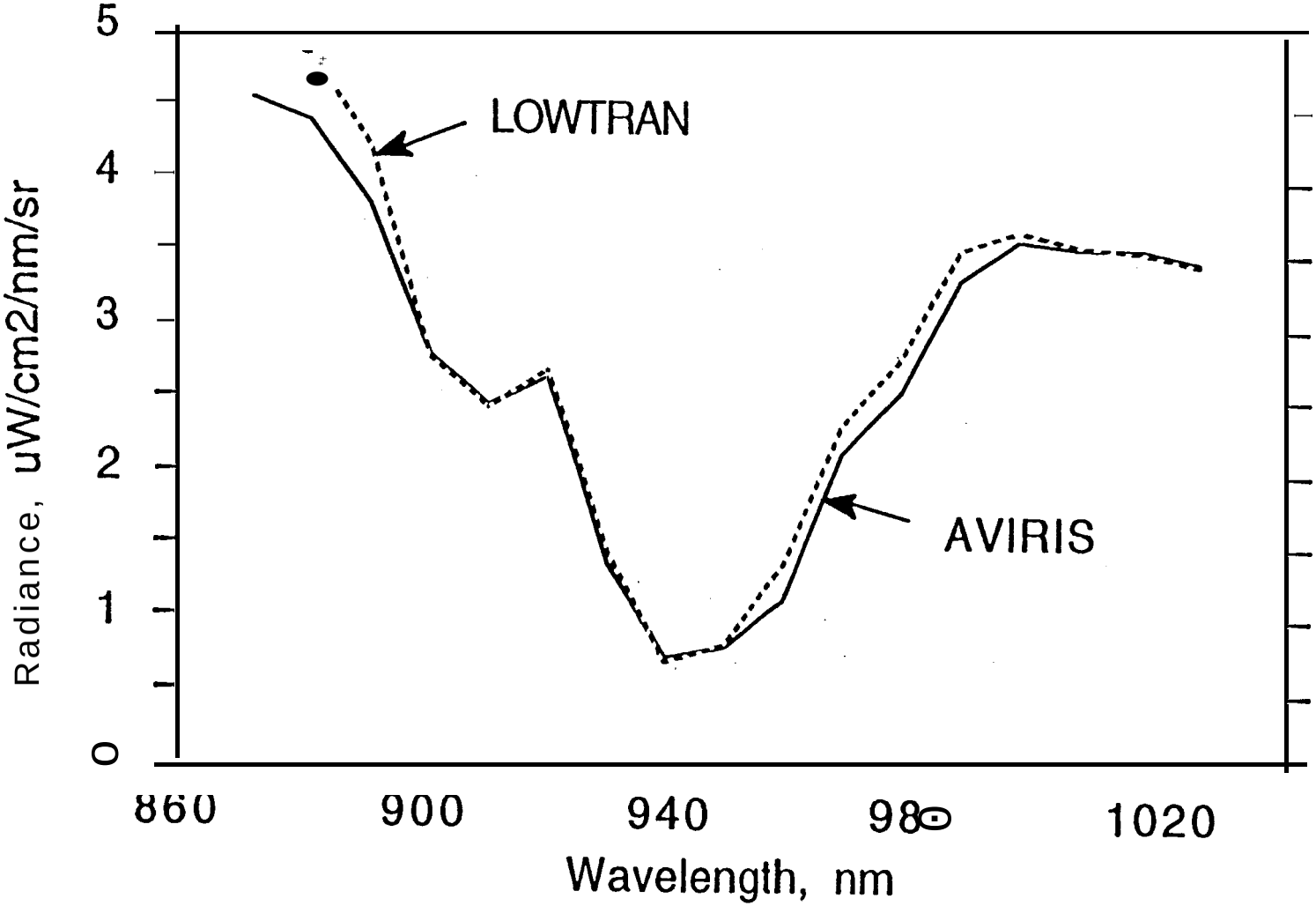
5
4
3
2
1
0
Radiance, uW/cm2/nm/sr
LOWTRAN
AVIRIS
860
900
940
980
1020
Wavelength, nm

Fig. 18

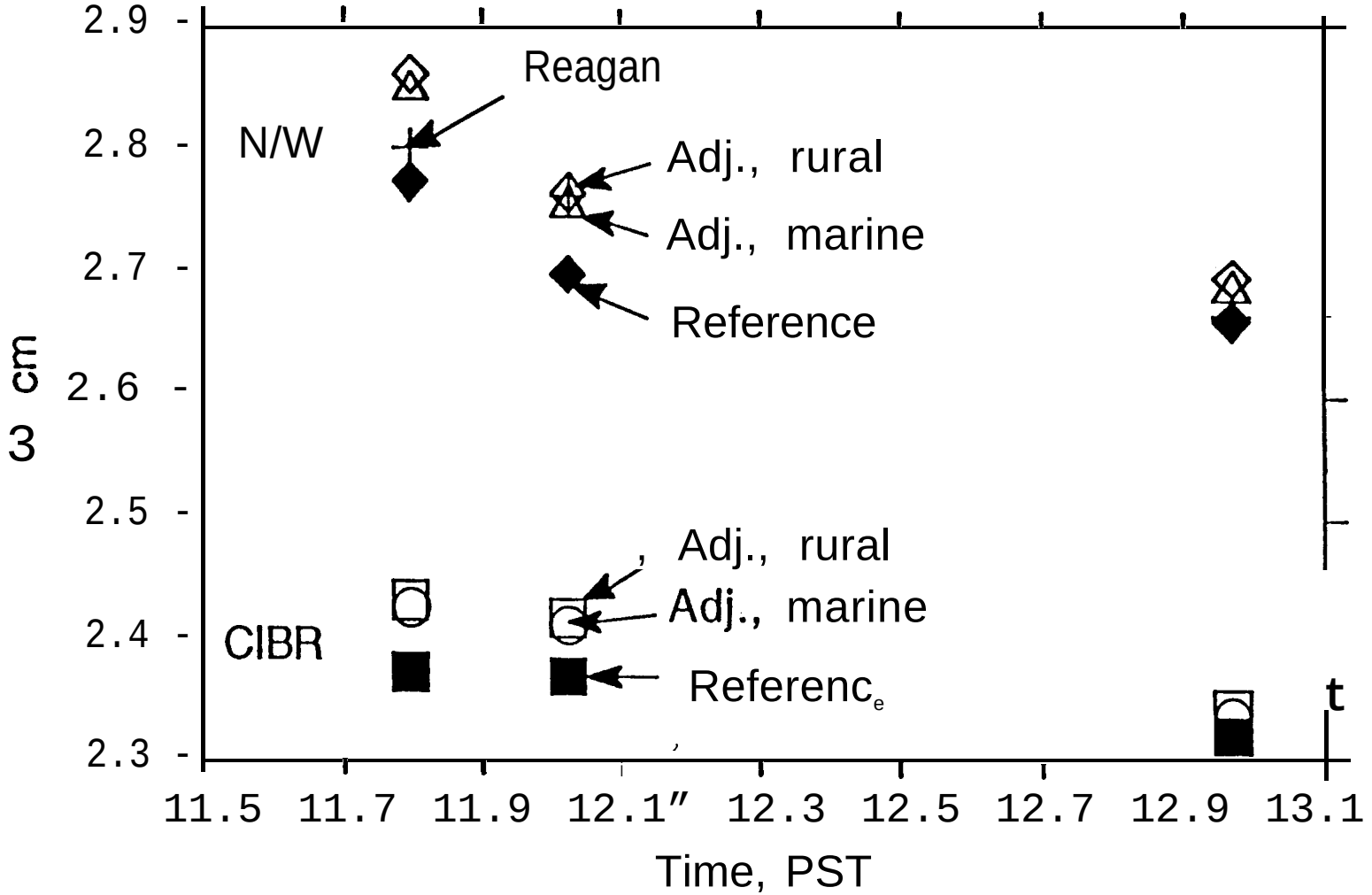
2.9
2.8
2.7
2.6
2.5
2.4
2.3
3 cm
Reagan
N/W
Adj., rural
Adj., marine
Reference
Adj., rural
Adj., marine
CIBR
Referenc$_e$
t
11.5
11.7
11.9
12.1″
12.3
12.5
12.7
12.9
13.1
Time, PST